

**APPLICATION OF FAST MARCHING METHODS FOR RAPID
RESERVOIR FORECAST AND UNCERTAINTY QUANTIFICATION**

A Thesis

by

FEYISAYO OMONIYI OLALOTITI-LAWAL

Submitted to the Office of Graduate Studies of
Texas A&M University
in partial fulfillment of the requirements for the degree of

MASTER OF SCIENCE

Chair of Committee, Akhil Datta-Gupta
Committee Members, Michael J. King
Bani Mallick
Head of Department, A. Daniel Hill

August 2013

Major Subject: Petroleum Engineering

Copyright 2013 Feyisayo Omoniyi Olalotiti-Lawal

ABSTRACT

Rapid economic evaluations of investment alternatives in the oil and gas industry are typically contingent on fast and credible evaluations of reservoir models to make future forecasts. It is often important to also quantify inherent risks and uncertainties in these evaluations. These ideally require several full-scale numerical simulations which is time consuming, impractical, if not impossible to do with conventional (Finite Difference) simulators in real life situations. In this research, the aim will be to improve on the efficiencies associated with these tasks. This involved exploring the applications of Fast Marching Methods (FMM) in both conventional and unconventional reservoir characterization problems.

In this work, we first applied the FMM for rapidly ranking multiple equi-probable geologic models. We demonstrated the suitability of drainage volume, efficiently calculated using FMM, as a surrogate parameter for field-wide cumulative oil production (FOPT). The probability distribution function (PDF) of the surrogate parameter was point-discretized to obtain 3 representative models for full simulations. Using the results from the simulations, the PDF of the reservoir performance parameter was constructed. Also, we investigated the applicability of a higher-order-moment-preserving approach which resulted in better uncertainty quantification over the traditional model selection methods.

Next we applied the FMM for a hydraulically fractured tight oil reservoir model calibration problem. We specifically applied the FMM geometric pressure approximation as a proxy for rapidly evaluating model proposals in a two-stage Markov Chain Monte Carlo (MCMC) algorithm. Here, we demonstrated the FMM-based proxy as a suitable proxy for evaluating model proposals. We obtained results showing a significant improvement in the efficiency

compared to conventional single stage MCMC algorithm. Also in this work, we investigated the possibility of enhancing the computational efficiency for calculating the pressure field for both conventional and unconventional reservoirs using FMM. Good approximations of the steady state pressure distributions were obtained for homogeneous conventional waterflood systems. In unconventional system, we also recorded slight improvement in computational efficiency using FMM pressure approximations as initial guess in pressure solvers.

DEDICATION

To my parents

ACKNOWLEDGEMENTS

I would like to express my utmost gratitude to my advisor, Dr. Datta-Gupta for his invaluable suggestions towards the completion of this research. Also, my appreciation goes to the MCERI research consortium for the financial support, without which this research would not have been completed.

I am likewise thankful to Dr. King for his insightful advice. It was also a great privilege to have Dr. Mallick as a member of my committee. For his encouraging words and moral support, I would also like to appreciate Dr. Awoleke. I owe great gratitude to Drs. Jiang Xie and Han Park, my senior colleagues and wonderful mentors.

Finally, to all my colleagues and seniors in the MCERI research group, I express my sincere appreciation for good and very useful suggestions that have helped tremendously through the completion of this work.

NOMENCLATURE

| | | |
|--------------------------------------|---|---|
| A_0 | = | Zero order pressure amplitude in Fourier domain |
| $A(r)$ | = | Surface area (ft^2) |
| B | = | Formation Volume Factor (RB / STB) |
| C_D, C_X | = | Data and parameter covariance matrices |
| C_k | = | Gaussian quadrature π polynomial coefficients |
| c_t | = | Total Compressibility ($/ psi$) |
| $DV(t)$ | = | Drainage volume surrogate ranking parameter (RB) |
| $\mathbf{d}_{obs}, \mathbf{d}_{sim}$ | = | Observed and Simulated data |
| h_f | = | Hydraulic fracture half-height (ft) |
| $k(\mathbf{x})$ | = | Spatially varying permeability (mD) |
| k_m, k_f | = | Matrix and fracture permeability (mD) |
| N | = | Number of PDF point discretization |
| $P(\bullet \bullet)$ | = | Conditional Probability Distribution |
| P_i | = | Model Weights |
| \mathbf{p}^n | = | Numerical pressure solution at the n^{th} time level |
| $p(\mathbf{x}, t)$ | = | Transient pressure field profile (psi) |
| $p^*(\mathbf{x}, t)$ | = | Approximate transient pressure field profile (psi) |
| $Q(\bullet \bullet)$ | = | Proposal distribution in the second stage of two-stage MCMC |

| | | |
|--------------------------|---|---|
| Q_w | = | Well Rate (BBL/D) |
| $q(\bullet \bullet)$ | = | Proposal distribution in MCMC (first stage of two-stage MCMC) |
| \mathbf{S} | = | Entropy vector |
| \mathbf{T} | = | Transmissibility matrix |
| $V_p(r)$ | = | Radially varying well drainage volume (BBL) |
| \mathbf{X} | = | Model parameter vector |
| \mathbf{x} | = | Spatial location (ft) |
| x_i | = | Surrogate parameter |
| x_f | = | Fracture half-length (ft) |
| $\alpha(\mathbf{x})$ | = | Hydraulic diffusivity |
| $\beta(\tau)$ | = | $\tau - t$ transformation factor |
| δ | = | Markov chain step size |
| ε_\bullet | = | Reservoir forecast error |
| μ | = | Fluid viscosity (cp) |
| ω | = | Frequency in Fourier domain |
| $\phi(\mathbf{x})$ | = | Spatially varying porosity |
| $\pi(\mathbf{X})$ | = | Posterior distribution (known within a normalizing constant) |
| $\pi(x)$ | = | Gaussian quadrature polynomial |
| $\rho(\bullet, \bullet)$ | = | MCMC acceptance probability |
| $\tau(\mathbf{x})$ | = | Diffusivity time of flight |
| ζ | = | Reservoir performance parameter |

TABLE OF CONTENTS

| | Page |
|---|------|
| ABSTRACT | ii |
| DEDICATION | iv |
| ACKNOWLEDGEMENTS | v |
| NOMENCLATURE | vi |
| TABLE OF CONTENTS | viii |
| LIST OF FIGURES | x |
| LIST OF TABLES | xiii |
| CHAPTER I INTRODUCTION | 1 |
| 1.1 Background | 1 |
| 1.2 The Asymptotic Solution to the Pressure Diffusivity Equation | 3 |
| 1.3 Study Objectives and Thesis Outline | 4 |
| CHAPTER II RAPID GEOLOGIC MODEL RANKING AND UNCERTAINTY QUANTIFICATION USING FAST MARCHING METHODS | 6 |
| 2.1 Introduction | 6 |
| 2.2 Methodology | 9 |
| 2.2.1 Drainage Volume Calculation Using Fast Marching Methods | 9 |
| 2.2.2 Model Selection for Multiple Realizations | 13 |
| 2.2.3 Uncertainty Quantification and Forecasts | 17 |
| 2.2.4 Workflow | 17 |
| 2.3 Illustration 1: A 2D Example | 18 |
| 2.4 Illustration 2: A 3D Example | 22 |
| 2.5 Discussion | 24 |
| 2.6 Summary | 28 |
| CHAPTER III RAPID TIGHT RESEVOIR MODEL CALIBRATION USING FAST MARCHING METHODS | 29 |
| 3.1 Introduction | 30 |

| | Page |
|--|--|
| 3.2 | Methodology 33 |
| 3.2.1 | Proxy Construction 33 |
| 3.2.2 | Bayesian Approach to Inverse Problems 36 |
| 3.2.3 | Problem Description 40 |
| 3.3 | Results and Discussion 47 |
| 3.4 | Summary 56 |
| CHAPTER IV CONCLUSIONS AND RECOMMENDATIONS 57 | |
| REFERENCES 60 | |
| APPENDIX A APPLICATION OF FAST MARCHING METHODS TO PRESSURE FIELD CALCULATIONS 67 | |
| A.1 | Procedure for Pressure Field Calculations using FMM 68 |
| A.1.1 | Drainage Volume Calculations with FMM 68 |
| A.1.2 | Geometric Pressure Approximation and Superposition in Space and Time 69 |
| A.1.3 | Derivation of Linear System of Equations for GMRES Solver 70 |
| A.2 | Results and Discussion 72 |
| A.2.1 | Steady State Pressure Solutions for Synthetic Waterflood Reservoir 73 |
| A.2.2 | Pressure Solutions for Unconventional (Tight) Reservoirs 79 |
| A.3 | Summary 81 |

LIST OF FIGURES

| | | Page |
|-------------|---|------|
| Figure 2.1 | Illustration of two dimensional upwind finite difference calculation | 11 |
| Figure 2.2 | Traditional model selection schemes: (a) P5-P50-P90 and (b) P10-P50-P90 schemes | 14 |
| Figure 2.3 | The general workflow | 18 |
| Figure 2.4 | (a) Permeability, (b) Porosity and (c) Diffusive time of flight profiles for one 2D model | 20 |
| Figure 2.5 | Rank correlation plot between DV and FOPT for the 2D case | 20 |
| Figure 2.6 | Cumulative oil production forecasts for the 2D case using (a) the P5-P50-P95 method, (b) the P10-P50-P90 method and (c) the Gaussian quadrature method | 21 |
| Figure 2.7 | (a) Permeability, (b) Porosity and (c) Diffusive time of flight profiles for one 3D model | 23 |
| Figure 2.8 | Rank correlation plots between DV and FOPT for the 3D case | 23 |
| Figure 2.9 | Cumulative oil production forecasts for the 3D case using (a) the P5-P50-P95 method, (b) the P10-P50-P90 method and (c) the Gaussian quadrature method | 25 |
| Figure 2.10 | Uncertainty analysis plots | 27 |
| Figure 3.1 | Hydraulically fractured reservoir model description showing (a) hydraulic fracture model with (b) an expanded view and (c) Enhanced Permeability Area (EPA) | 42 |
| Figure 3.2 | History matching problem set-up showing (a) the reference model, (b) the starting (base) model and (c) the simulated responses of both models | 43 |
| Figure 3.3 | The two-stage MCMC algorithm flow chart | 45 |

| | Page |
|-------------|--|
| Figure 3.4 | Logarithm of $\tau(\mathbf{x})$ contours and cross plots comparing pressure calculations between proxy and finite difference for the reference model [(a) and (b)], the lower extreme model [(c) and (d)] and the higher extreme model [(e) and (f)] 46 |
| Figure 3.5 | Single stage MCMC performance showing plots of the (a) misfit and (b) acceptance rate with iterations 48 |
| Figure 3.6 | History matching results using the single stage MCMC algorithm showing (a) initial spread in responses, (b) final spread in responses, and boxplots depicting (c) initial parameter uncertainty and (d) final parameter uncertainty 49 |
| Figure 3.7 | Two-stage MCMC performance showing plots of the (a) misfit and (b) acceptance rate with iterations 51 |
| Figure 3.8 | History matching results using the two-stage MCMC algorithm showing (a) initial spread in responses, (b) final spread in responses, and boxplots depicting (c) initial parameter uncertainty and (d) final parameter uncertainty 52 |
| Figure 3.9 | Entropy plots 54 |
| Figure 3.10 | Graphical summary of history matching results showing (a) the EPA and logarithm of $\tau(\mathbf{x})$ for the reference model, (b) the EPA and logarithm of $\tau(\mathbf{x})$ for the base model, (c) logarithm of $\tau(\mathbf{x})$ for 4 models sampled from the posterior distribution 55 |
| Figure A.1 | Conventional reservoir test case set up showing (a) the waterflood pattern applied to both homogeneous and heterogeneous reservoirs and (b) well flow rate schedule 73 |
| Figure A.2 | Steady state FMM-approximate and GMRES-refined pressure solutions for homogeneous 5-spot waterflood pattern 74 |
| Figure A.3 | Material balance errors in FMM-approximate and GMRES-refined pressure solutions for homogeneous 5-spot waterflood pattern 75 |
| Figure A.4 | Heterogeneous model: (a) permeability distribution on logarithmic scale, (b) porosity distribution 76 |

| | Page |
|------------|--|
| Figure A.5 | Steady state FMM-approximate and GMRES-refined pressure solutions for heterogeneous 5-spot waterflood pattern 77 |
| Figure A.6 | Material balance errors in FMM-approximate and GMRES-refined pressure solutions for heterogeneous 5-spot waterflood pattern 78 |
| Figure A.7 | Pressure solutions for a tight oil reservoir showing (a) FMM geometric approximation pressure distribution, (b) pressure distribution obtained from ECLIPSE [®] , (c) GMRES pressure solution with $p_0(\mathbf{x},t) = p_{init}$, and (d) GMRES pressure solution with $p_0(\mathbf{x},t) = p^*(\mathbf{x},t)$ 80 |
| Figure A.8 | Comparative GMRES computational time between cases: $p_0(\mathbf{x},t) = p_{init}$ and $p_0(\mathbf{x},t) = p^*(\mathbf{x},t)$ 81 |

LIST OF TABLES

| | Page |
|--|------|
| Table 2.1 Error quantification for the 2D Case | 22 |
| Table 2.2 Error quantification for the 3D Case | 24 |
| Table 3.1 List of model parameters | 44 |

CHAPTER I

INTRODUCTION

1.1 Background

An important task for reservoir engineers is to make reliable forecasts of field performance measures such as the cumulative field hydrocarbon production and associated uncertainties. Quantifying these uncertainties requires, first characterizing the reservoir including understanding the geology, estimating the property distribution such as permeability, porosity, water saturation, fault location and geometry and so on (Al-Khalifa, 2004). These estimations are assisted using data sets obtained from careful measurements made from the reservoir being evaluated. However, the multiscale nature of these data sets and also possibility of measurement errors in data, which are common occurrences in real life scenarios, complicates the forecasting and uncertainty quantification procedures.

For decades, stochastic approaches have been an important tool for characterizing uncertainties in reservoir geologic models. It usually involves generating multiple equally probable geologic models for evaluation based on a specified reservoir performance parameter. With this, the variance of the parameter for all the models (a measure of uncertainty), may be assessed. Integrating available production data into existing reservoir models, in an approach referred to as model calibration or history matching, also helps to further reduce the current level of uncertainty (Oliver et al., 2008).

Ideally, several full scale simulations are required to evaluate all geologic models and to integrate production data. However for high resolution geologic models, these procedures get

very computationally expensive and most times, impractical. Getting around this has, over the years, sprung up an active research area in approximate simulator development. These simulators, also known as proxies, are applied in estimating specific reservoir performance measures very efficiently. Proxies have been applied extensively to significantly improve the efficiencies in geologic model ranking (Graf et al., 2011; Hird and Dubrule, 1998; Idrobo et al., 2000; Kim and Dobin, 2008; Shook and Mitchell, 2009) and history matching (Luo et al., 2011; Mohaghegh et al., 2012; Srinivasan and Caers, 2000; Yin et al., 2011).

A new proxy recently applied by Yin et al. (2011) for shale gas model calibration involves the application of a drainage volume estimator using the Fast Marching Method (FMM) (Sethian, 1999). The FMM is a class of front tracking algorithm that has long been applied in wave propagation (Fatemi et al., 1995), subsurface and medical imaging. For porous media flow, the Eikonal equation can be arrived at by retaining the high frequency terms of the asymptotic expansion of the pressure diffusivity equation (Datta-Gupta et al., 2001). The FMM has been applied to solving the Eikonal equation to efficiently obtain the diffusive time of flight contours, (a measure of pressure front arrival time), leading to a quick method for calculating drainage volumes in both homogeneous and heterogeneous reservoirs (Datta-Gupta et al., 2011). Apart from history matching problems, the drainage volume concept has also been applied in quantitative well placement (Hosseini et al., 2010) and fracture stage optimization (Sehbi et al., 2011), in a streamline framework.

In this chapter, we first review the concept of the asymptotic solution of the pressure diffusivity equation which leads to the Eikonal equation. Next, the study objectives and outline of this thesis will be discussed.

1.2 The Asymptotic Solution to the Pressure Diffusivity Equation

Pressure diffusion in porous media may be modeled by the well-known pressure diffusivity equation given as (Lee et al., 2003):

$$\phi(\mathbf{x})\mu c_t \frac{\partial p(\mathbf{x}, t)}{\partial t} = \nabla \cdot (k(\mathbf{x})\nabla p(\mathbf{x}, t)) \quad (1.1)$$

where $p(\mathbf{x}, t)$ represents the spatial distribution of the pressure response in the porous media, $k(\mathbf{x})$ and $\phi(\mathbf{x})$ represent the spatial distribution of permeability and porosity and μ and c_t denote the fluid viscosity and medium total compressibility. In the Fourier domain **Eq. (1.1)** becomes:

$$\phi(\mathbf{x})\mu c_t (-i\omega)\tilde{p}(\mathbf{x}, \omega) = k(\mathbf{x})\nabla^2 \tilde{p}(\mathbf{x}, \omega) + \nabla k(\mathbf{x})\nabla \tilde{p}(\mathbf{x}, \omega) \quad (1.2)$$

The asymptotic solution method here has been extensively used in geometric optics and seismology (Virieux et al., 1994). The method exploits an analogy between a propagating pressure front and a propagating wavefront. For diffusive pressures, an asymptotic expansion follows if we consider a solution in terms of inverse powers of $\sqrt{-i\omega}$ (Datta-Gupta et al., 2001):

$$\tilde{p}(\mathbf{x}, \omega) = e^{-\sqrt{-i\omega}\tau(\mathbf{x})} \sum_{k=0}^{\infty} \frac{A_k(\mathbf{x})}{(\sqrt{-i\omega})^k} \quad (1.3)$$

where $\tau(\mathbf{x})$ is the ‘phase’ of the wave representing the geometry of a propagating front. It is called the diffusive time of flight – a measure of pressure front arrival time. Also, $A_k(\mathbf{x})$ is pressure amplitude at k^{th} order. A solution of the above form can be interpreted on physical grounds based on the scaling behavior of diffusive flow. The high frequency solution is given by the initial terms of the asymptotic series and will correspond to the propagation of a ‘pressure

front'. We, therefore, consider a solution of the form;

$$\tilde{p}(\mathbf{x}, \omega) = A_0(\mathbf{x})e^{-\sqrt{-i\omega}\tau(\mathbf{x})} \quad (1.4)$$

Inserting **Eq. (1.4)** into **Eq. (1.2)**, and collecting the terms of the highest order in $\sqrt{-i\omega}$, that is $(\sqrt{-i\omega})^2$, the result is the Eikonal equation given as:

$$\sqrt{\alpha(\mathbf{x})}|\nabla\tau(\mathbf{x})|=1 \quad (1.5)$$

where $\alpha(\mathbf{x})$ is the diffusivity given by:

$$\alpha(\mathbf{x}) = \frac{k(\mathbf{x})}{\phi(\mathbf{x})\mu c_t} \quad (1.6)$$

From **Eq. (1.5)** the diffusivity can be interpreted as the speed function in the Eikonal equation. This means that the speed of pressure front propagation is governed by the diffusivity in **Eq. (1.6)** which is a function of both reservoir and fluid properties. Therefore the diffusive time of flight $\tau(\mathbf{x})$ calculated by solving Eq. (1.5), qualifies as a dynamic measure of reservoir performance and will be applied in the efficient calculation of drainage volumes using a Fast Marching Method (FMM) for geologic model ranking and uncertainty quantification in the next chapter of this thesis.

1.3 Study Objectives and Thesis Outline

The objective of this work is to investigate the applicability of Fast Marching Methods (FMM) in rapid hydrocarbon reservoir forecasts under uncertainty. We apply the FMM concept in the ranking of multiple geologic models as well as in the tight oil reservoir model calibration problem, the details of which are presented in Chapters II and III of this thesis. We also

investigated the application of the FMM concept to enhance the computational speed in pressure field calculations for both conventional and unconventional reservoirs. Details of this will, however, be presented in the Appendix A section of this thesis.

CHAPTER II

RAPID GEOLOGIC MODEL RANKING AND UNCERTAINTY QUANTIFICATION USING FAST MARCHING METHODS

The focus in this chapter is on the application of Fast Marching Methods (FMM) as a tool for quickly ranking geologic models in order to reveal inherent uncertainties for educated decision making on ‘green’ asset development options. Here, we rank all reservoir model realizations based on the field cumulative oil production (FOPT) in the primary recovery phase over a certain period of time. To speed up the process, the drainage volume was estimated for each model using the FMM and then applied as a surrogate parameter for the FOPT. In the model selection process, we discretize the probability distribution function (PDF) of the surrogate parameter to obtain three models used to approximate the final PDF of the FOPT.

2.1 Introduction

Significant uncertainties exist in petroleum exploration investment decisions which can be primarily tied to uncertainties in subsurface model parameters. Uncertainties abound in the spatial distribution of static and dynamic properties such as porosity, permeability, phase saturations, phase contacts, fault structures, facies distribution, and so on. These uncertainties may be reduced as more data such as well log, well test, production and seismic data get integrated into existing geologic models (Hu et al., 1999). However, these data sets typically are either of low resolution (well test and seismic data) or too local and sparse (well logs) to remove substantial amount of uncertainties (Shook and Mitchell, 2009). Moreover, these data sets are often times very limited, especially at the initial stages of ‘green’ field development plans.

Geostatistical methods have widely been adopted as an important tool in geologic modeling and uncertainty quantification (Hu et al., 1999; Journel, 1990). This generally involves generating multiple equi-probable realizations of models that satisfy the (limited) available information. Ideally, all models are evaluated by running full simulations, and inherent uncertainties quantified based on a specific reservoir performance parameter. The downside of this rigorous Monte Carlo approach is the prohibitive computational expense for real life scenarios.

Getting around this problem has instigated evaluating geologic models using algorithms/simulators which approximate models responses and thus, lead to computationally efficient means of ranking these models (Deutsch and Srinivasan, 1996). These approximate schemes have evolved over time, starting from the Dykstra-Parsons method of characterizing and ranking model permeability heterogeneities (Johnson Jr, 1956). Alabert and Modot (1992) proposed a ranking method based on connected pore volumes around the wells, but this method was later shown in a waterflood system to give poor correlations with oil recovery factor which was the measure of reservoir performance (Saad et al., 1996). Hird and Dubrule (1998) on the other hand, proposed the drainable Hydrocarbon Pore Volume (HCPV) concept based on a Resistivity Index (RI) method which was well correlated with ultimate recovery. This method has been acclaimed useful for primary recovery ranking purposes (Shook and Mitchell, 2009).

On the secondary recovery ranking methods, Hirsch and Schuette (1999) proposed a ranking approach looking at the permeability connectivity from the graph theory perspective, using a shortest path algorithm. Kim and Dobin (2008) similarly in the graph theory framework, considered a Fast Marching Method (FMM); taking the absolute permeability-porosity ratio as the speed function. These methods pay more attention to static properties and so are only limited to very simple cases. Recent advances in streamline simulation (Datta-Gupta and King, 2007)

has however helped in incorporating more realism to ranking models for waterflood projects. Idrobo et al. (2000) and Mishra et al. (2000) applied thresholds to the convective time-of-flight contour to estimate volumetric sweep efficiency, E_v which was used as a surrogate parameter for ranking multiple geologic models. Similarly, Shook and Mitchell (2009) proposed a model ranking approach that uses the E_v as the surrogate parameter which was however calculated using only the dynamic flow capacity.

The probability distribution functions (PDF) of the surrogate performance parameter can be obtained from the model ranking process, as suggested by Deutsch and Srinivasan (1996), and these have proved useful in representing the PDF of the main reservoir performance parameter. In most cases, the two PDF should be reasonably similar if the ‘proxies’ adopted for ranking are sufficiently good. The reservoir performance parameter PDF can be approximated by careful selection of certain models which preserve important characteristics of the distribution (Deutsch and Srinivasan, 1996). This concept was adopted by Idrobo et al. (2000) and Mishra et al. (2000) in selecting three representative models from the E_v distribution for full scale simulations. These simulations provided the Recovery Factor, R_F for the selected models and these were used in constructing the PDF of R_F for all the ensemble of models. In their work, two PDF discretization schemes were considered: the P5-P50-P95 and P10-P50-P90. That is, the 5th, 50th and 95th percentiles of the surrogate parameter distribution are selected for full simulation in the first scheme while the 10th, 50th and 90th percentiles are selected for the second. These pre-defined PDF discretization methods work well under Gaussian assumptions. However, the approach is inadequate when distributions are non-Gaussian and tend to under-estimate moments of the original distribution (Miller and Rice, 1983). These authors proposed a Gaussian quadrature approach for approximating a PDF in which N points are selected and their

corresponding weights calculated simultaneously such that the first $2N - 1$ moments of the PDF are preserved. This approach has gained wide applicability in geotechnical reliability (Christian and Baecher, 1999) and many other engineering fields.

The objective of this chapter is twofold: First, we propose a new way of rapidly ranking multiple geologic models under primary depletion using the drainage volume as the surrogate parameter. These drainage volumes are estimated by solving the Eikonal equation (Xie, Gupta, et al., 2012) which results from the asymptotic expansion of the pressure diffusivity equation (Datta-Gupta et al., 2001; Vasco et al., 2000) as shown in Chapter I. For each model, the drainage volume was computed in seconds using the Fast Marching Method (FMM) (Sethian, 1996, 1999). Second, the Gaussian quadrature (higher-order-moment-preserving PDF discretization) approach which is applied as a model selection method is compared with the traditional model selection methods.

2.2 Methodology

2.2.1 Drainage Volume Calculation using Fast Marching Methods

Recall from Chapter I the Eikonal equation derived from the pressure diffusivity equation:

$$\sqrt{\alpha(\mathbf{x})} |\nabla \tau(\mathbf{x})| = 1 \quad (1.5)$$

where $\alpha(\mathbf{x})$ is the diffusivity given by:

$$\alpha(\mathbf{x}) = \frac{k(\mathbf{x})}{\phi(\mathbf{x})\mu c_f} \quad (1.6)$$

The Eikonal equation may be solved using a class of front tracking methods called the Fast Marching Methods (Xie, Gupta, et al., 2012) to obtain a scalar field of the diffusive time of flight

$\tau(\mathbf{x})$. In 2-D Cartesian grids, **Eq. (1.5)** is discretized using a simple five-point upwind finite difference scheme to obtain:

$$\max(D_{i,j}^{-x}\tau, -D_{i,j}^{+x}\tau, 0)^2 + \max(D_{i,j}^{-y}\tau, -D_{i,j}^{+y}\tau, 0)^2 = 1/\alpha \quad (2.1)$$

where D is the gradient approximated with a 1st order finite difference scheme given by:

$$\text{along x-direction: } D_{i,j}^{-x}\tau = \frac{\tau_{i,j} - \tau_{i-1,j}}{\Delta x}; \quad D_{i,j}^{+x}\tau = \frac{\tau_{i+1,j} - \tau_{i,j}}{\Delta x} \quad \text{and} \quad (2.2a)$$

$$\text{along y-direction: } D_{i,j}^{-y}\tau = \frac{\tau_{i,j} - \tau_{i,j-1}}{\Delta y}; \quad D_{i,j}^{+y}\tau = \frac{\tau_{i,j+1} - \tau_{i,j}}{\Delta y} \quad (2.2b)$$

As an illustration, consider a two dimensional domain shown in **Fig. 2.1**. Assuming the τ values are known at points C and D (that is the pressure front has just reached these points), to obtain the τ value at black colored node **Eq. (2.1)** can be written as:

$$\left(\frac{\tau_C - \tau}{\Delta x}\right)^2 + \left(\frac{\tau_D - \tau}{\Delta y}\right)^2 = \frac{1}{\alpha} \quad (2.3)$$

Thus, τ can be calculated very efficiently. It can be observed that the upwind finite difference approximation of the FMM algorithm possess a causality relationship, which means that the value at each node depends only on smaller adjacent values.

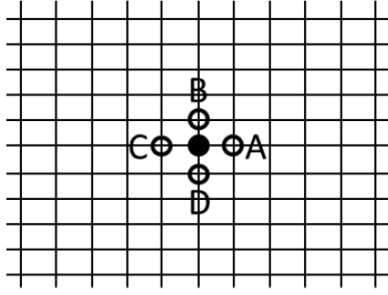


Figure 2.1: Illustration of two dimensional upwind finite difference calculation (Xie, Gupta, et al., 2012)

Generally in the FMM algorithm, all nodes are characterized as *accepted*, *neighbor* and *far away* depending on the progress of calculations. At the start of the algorithm, starting nodes are labeled *accepted* and assigned zero τ values. All adjacent nodes are labeled *neighbor* and the rest of the nodes in the domain are labeled as *far away*. The *far away* nodes are assigned τ values of infinity. The following steps are carried out to calculate the τ values for the whole field:

- Using the known τ values in the accepted nodes calculate the τ values for all adjacent *neighbor* nodes using the approach described in **Eq. (2.1)** to **(2.3)**.
- Pick the node with the least τ value and label it *accepted*, then label all its adjacent points (some of which were initially categorized as *far away*) *neighbor*.
- Repeat the first two steps until all nodes have been labeled *accepted*.

The FMM algorithm runs very efficiently and the $\tau(\mathbf{x})$ contours are obtained for large number of nodes in seconds. To improve the accuracy along diagonal directions however, we adopt the Multi-Stencil Fast Marching (MSFM) method proposed by Hassouna and Farag (2007), which uses eight stencils on the Cartesian grid.

With the assumption that the contours $\tau(\mathbf{x})$ are coincide with pressure contours, the radius of investigation is defined and the drainage volume can be estimated at any time t as follows (Xie, Gupta, et al., 2012):

$$DV(t) = \sum_{i,j,k} V_{i,j,k} \phi_{i,j,k} \theta \left(t - \frac{\tau_{i,j,k}^2}{2n} \right) \quad (2.4)$$

where n represents the number of dimensions of the domain, $V_{i,j,k} \phi_{i,j,k}$ is the pore volume of grid cell (i, j, k) and θ is the Heaviside function given as:

$$\theta(t - \chi) = \begin{cases} 1; & t \geq \chi \\ 0; & t < \chi \end{cases} \quad (2.5)$$

In other words, we sum up the pore volume of the grid cells within the radius of investigation at a time t of interest. The drainage volume provides a clear measure of the connected volume between the reservoir and the wells. The main advantage of this approach is the speed at which the drainage volumes are calculated using the FMM. The drainage volume calculations for an ensemble of 200 models considered in the 2-D case (presented later in this chapter) took about 30 seconds on a simple personal computer. On the same computer, the same ensemble of models required more than 3 hours for full-scale finite difference simulation. In this work, we demonstrated the possibility of fast drainage volume calculations using the FMM for multiple model realizations in 2-D and 3-D synthetic cases. For each case, the PDF of the drainage volumes was discretized using approaches discussed in the following section.

2.2.2 Model Selection for Multiple Realizations

The idea here is to approximate the true PDF of the actual reservoir performance parameter ζ with few representative models selected from the PDF of the surrogate parameter x . Using the cumulative density function (CDF) constructed from the PDF of x , specific percentiles, corresponding to certain models may be selected for full simulation. These models are normally weighted in the eventual reconstruction of the PDF of ζ after full simulations. In most PDF point discretization routines, these weights are calculated such that the first few moments of the distribution are preserved by the selected models. In this work, we consider two approaches for model selection: First, the *traditional* method whereby pre-determined percentiles are first obtained from the CDF of x , then their corresponding weights calculated (Mishra et al., 2000); and second, a *Gaussian quadrature* approach which simultaneously selects appropriate models and calculates their corresponding weights (Miller and Rice, 1983).

The Traditional Approach

This approach has become a standard for geologic uncertainty quantification in field development projects (Idrobo et al., 2000; Mishra et al., 2000). Two popular forms are the P5-P50-P95 and the P10-P50-P90 methods; the latter being more popular. This simply means that, the 5th, 50th and the 95th percentiles are selected from the CDF of x in the first method, and the 10th, 50th and the 90th percentiles in the second as shown in **Fig. 2.2**. Calculating the weights P_i requires solving the following set of equations (Mishra et al., 2000):

$$\sum_{i=1}^3 P_i = 1 \quad (2.6)$$

$$\sum_{i=1}^3 P_i x_i = E[x] \quad (2.7)$$

$$\sum_{i=1}^3 P_i x_i^2 = \text{var}[x] + E^2[x] \quad (2.8)$$

For the purpose of this work, x in these equations refers to the drainage volume of each model at a specific time. It is worth noting that the first and second order moments are preserved by Eqs. (2.7) and (2.8) while Eq. (2.6) only ensures that all weights sum up to unity.

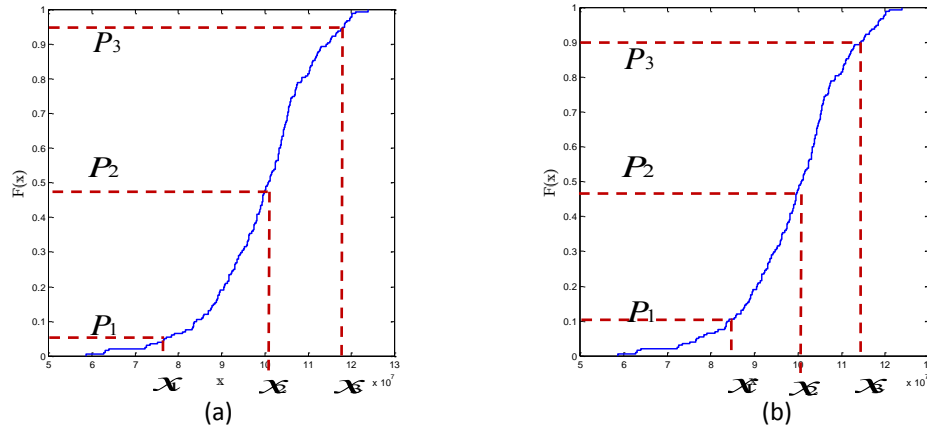


Figure 2.2: Traditional model selection Schemes: (a) P5-P50-P90 and (b) P10-P50-P90 schemes

The Gaussian Quadrature Approach

The traditional method gives good results (approximated PDFs similar to true PDFs) under the assumptions that the probability distributions of interest are Gaussian. However, higher order moments normally need to be preserved in model selection method to sufficiently approximate non-Gaussian distributions. To solve this problem, the Gaussian quadrature approach was proposed. According to (Rosenblueth and Hong, 1987), using Gaussian quadrature, it is possible

to find N percentiles that replace the PDF of a random variable X while simultaneously matching $2N-1$ of its moments. The approach as described by (Miller and Rice, 1983) is presented as follows.

In this approach, the first k^{th} order moments of a PDF $p(x)$ may be approximated with only N points on the PDF weighted by P_i using the following set of equations:

$$E[x^k] = \int_{-\infty}^{\infty} x^k p(x) dx = \sum_{i=1}^N P_i x_i^k ; \text{ for } k = 0, 1, 2, \dots, 2N-1 \quad (2.9)$$

This generates a set of $2N-1$ moment equations in which both P_i and x_i are unknown for all k .

The steps followed to solve for the unknowns are outlined below:

- First, we can define an arbitrary polynomial $\pi(x) = \prod_{i=1}^N (x - x_i) = \sum_{k=0}^N C_k x^k$, setting $C_N = 1$

and $\pi(x_i) = 0 \quad \forall i \in [1, N]$; where N is the number of PDF discretization points.

- Let us consider the first $N+1$ equations of **Eq. (2.9)** which describes the first N moments.

In other words, the equation $(k+1)$ defines the k^{th} moment equation. We can multiply

each equation by the corresponding C_k as described below:

$$\begin{aligned} C_0 &\times \{P_1 x_1^0 + P_2 x_2^0 + \dots + P_N x_N^0 = E[x^0] = 1\} \\ C_1 &\times \{P_1 x_1^1 + P_2 x_2^1 + \dots + P_N x_N^1 = E[x^1]\} \\ &\vdots \quad \quad \quad \vdots \quad \quad \quad \vdots \quad \quad \quad \vdots \quad \quad \quad \vdots \\ C_N &\times \{P_1 x_1^N + P_2 x_2^N + \dots + P_N x_N^N = E[x^N]\} \end{aligned} \quad (2.10)$$

- Adding column-wise the system of equations in **Eq. (2.10)** we obtain the following: In other words, the equation $(k + 1)$ defines the k^{th} moment equation. We can multiply

$$\sum_{i=1}^N P_i \left(\sum_{k=0}^N C_k x_i^k \right) = \sum_{i=1}^N P_i \pi(x_i) = \sum_{k=0}^N C_k E[x^k] \quad (2.11)$$

Note that the last term of **Eq. (2.11)** represents the Right Hand Side (RHS) of the equation obtained from the previous step and the first two terms represent the Left Hand Side (LHS) which vanishes by the definition of the polynomial $\pi(x)$. Therefore, from the first $N + 1$ equations of **Eq. (2.9)**, we obtain the following equation:

$$\sum_{k=0}^N C_k E[x^k] = C_0 E[x^0] + C_1 E[x^1] + \dots + C_N E[x^N] = 0 \quad (2.12)$$

- We can repeat the second and third steps for equations from the 2^{nd} to $(N + 2)^{th}$ equations of **Eq. (2.9)** to obtain:

$$\sum_{k=0}^N C_k E[x^{k+1}] = C_0 E[x^1] + C_1 E[x^2] + \dots + C_N E[x^{N+1}] = 0 \quad (2.13)$$

- This is continued until the last set of $N + 1$ equations of **Eq. (2.9)**; that is from the $(N - 1)^{th}$ to the $(2N - 1)^{th}$ equation to obtain:

$$\sum_{k=0}^N C_k E[x^{k+N-1}] = C_0 E[x^{N-1}] + C_1 E[x^{N-1}] + \dots + C_N E[x^{2N-1}] = 0 \quad (2.14)$$

- Noting that $C_N = 1$ by definition, these result in a $N \times N$ system of equations with C_k as the unknowns. Therefore we can obtain the coefficients C_k of the polynomial $\pi(x)$.
- Then, the discretization points in the PDF x_i can be obtained as the roots of $\pi(x)$.
- Substituting x_i 's into the linear system in **Eq. (2.9)**, we obtain the corresponding weights P_i .

2.2.3 Uncertainty Quantification and Forecasts

Once the models have been selected and their corresponding weights calculated, full simulations are run for each selected realization R_i to obtain the field performance parameter $\zeta(R_i)$ of interest with which the forecast is made. The forecast of the reservoir performance parameter $\zeta(R_i)$ typically requires calculating the mean and standard deviation (a measure of uncertainty) of ζ as follows (Mishra et al., 2000):

$$E[\zeta] = \sum_{i=1}^N P_i \zeta(R_i) \quad (2.15)$$

$$\sigma(\zeta) = \left\{ \sum_{i=1}^N \left\{ P_i (\zeta(R_i) - E[\zeta])^2 \right\} \right\}^{1/2} \quad (2.16)$$

2.2.4 Workflow

A graphic description of proposed method for geologic model ranking and uncertainty quantification is presented in **Fig. 2.3**. The drainage volume (DV), which was considered the surrogate measure of reservoir performance, was calculated for each realization using the FMM. A distribution of the DV was then generated from which a few models were selected and their corresponding weights calculated using each of the methods previously described. Full simulations were performed on the selected models using the ECLIPSE[®] to determine the measure of reservoir performance ζ_i which, for the purpose of the study, was the field-wide cumulative oil production (FOPT). Using the calculated weights, uncertainties in the forecast were quantified. The forecasts were also compared with Monte Carlo results to validate the accuracy of the new model ranking and uncertainty quantification method.

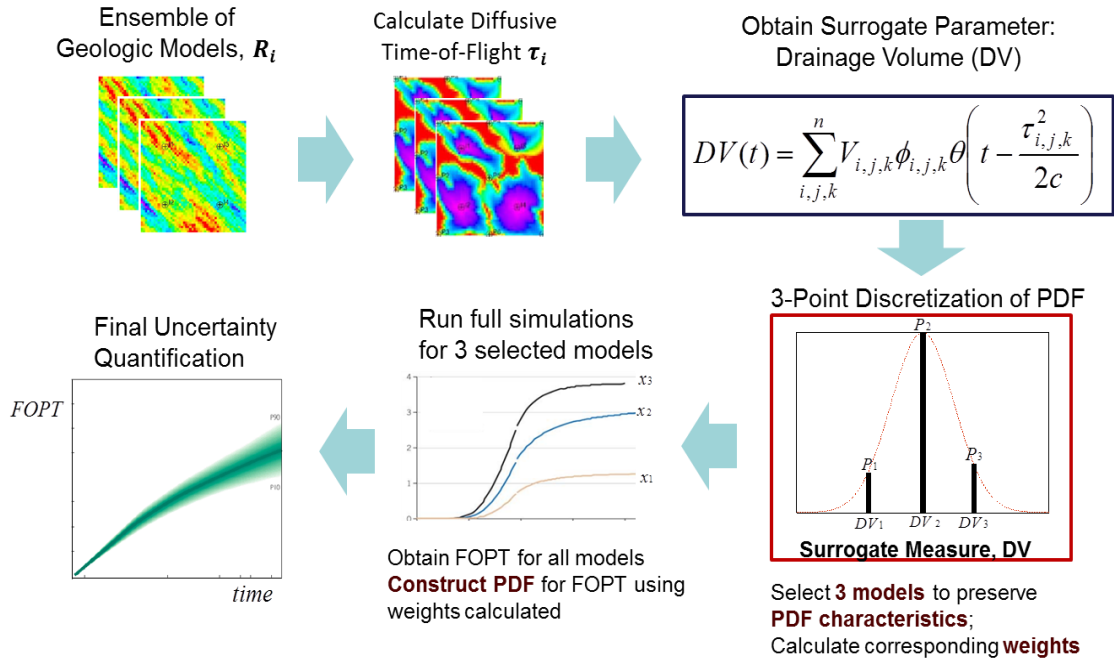


Figure 2.3: The general workflow

2.3 Illustration 1: A 2D Example

In this case 200 geostatistical realizations were generated using Sequential Gaussian Simulation (Remy, 2005), varying both permeability and porosity. The reservoir was discretized into 125×110 Cartesian grids each of size $100 \times 100 \times 100$ ft. The reservoir permeability with log-scale average value of approximately 1.2 and porosity with average value of approximately 21%, as shown in **Fig. 2.4(a)**, both having 45° azimuthal trend.

The reservoir has uniform initial pressure of 4000 psi and four producers, each maintained at 1000 psi bottom hole pressure and arranged as shown in **Fig. 2.4**. The goal here was to rank all models based on the FOPT over a period of 30 years of primary production. The FMM was applied to calculate the drainage volumes of each model in the ensemble and a threshold pressure front arrival time of 100 days was applied on the drainage volume for the purpose of

ranking the models. The choice of the cut-off time here is based on the inception of significant interference among the wells as depicted in **Fig. 2.4 (c)**. To confirm the suitability of the drainage volume at the specified cut-off time, the rank correlation with the FOPT after 30 years of production (obtained by running full simulations for all models) was calculated to be 0.92 as shown in **Fig. 2.5**. With a value close to 1 the suitability of the surrogate parameter was confirmed.

Model selections were made for full simulation using the methods discussed: the P5-P50-P95, P10-P50-P90 and the Gaussian quadrature. Full simulation was run on all selected models using the ECLIPSE[®] reservoir simulator to obtain the FOPT up to a period of 30 years. Then uncertainties were quantified from the results of the simulations by estimating the mean and standard deviation of the FOPT obtained using **Eqs. (2.15)** and **(2.16)**. **Fig. 2.6 (a)** through **(c)** compare the forecast results obtained from the proposed ranking methodology, using the three model selection methods, with those from the Monte Carlo method. In each of the plots, the mean and standard deviation of the FOPT obtained through Monte Carlo simulation is labeled as the ‘True mean’ and ‘True STD’ respectively while the ‘Calculate mean’ and ‘Calculated STD’ labels respectively represent the mean and standard deviation of the FOPT obtained using the newly proposed model ranking and uncertainty quantification methods. From these plots it clear that the Gaussian Quadrature method resulted in the best uncertainty forecast of the FOPT compared with the traditional methods. For more objective inference, the errors between the estimated mean \mathcal{E}_{mean} and standard deviation \mathcal{E}_{std} and those obtained by Monte Carlo simulation were quantified for each of the methods. The calculations were carried out using **Eq. (2.17)** and **(2.18)**.

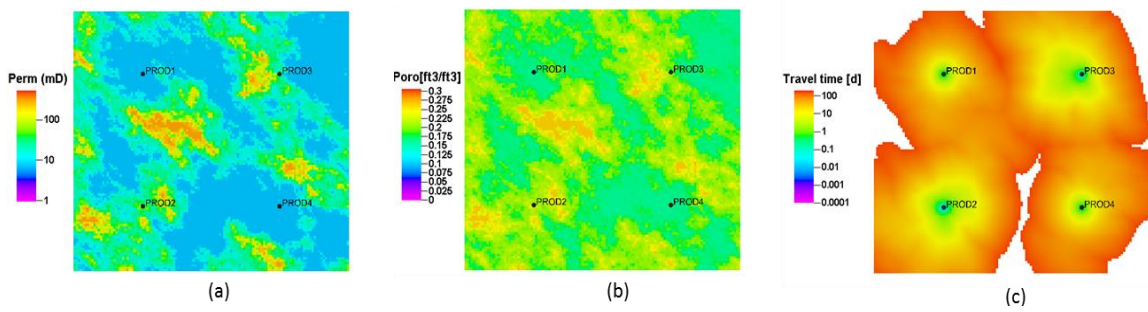


Figure 2.4: (a) Permeability, (b) Porosity and (c) Diffusive time of flight profiles for one 2D model

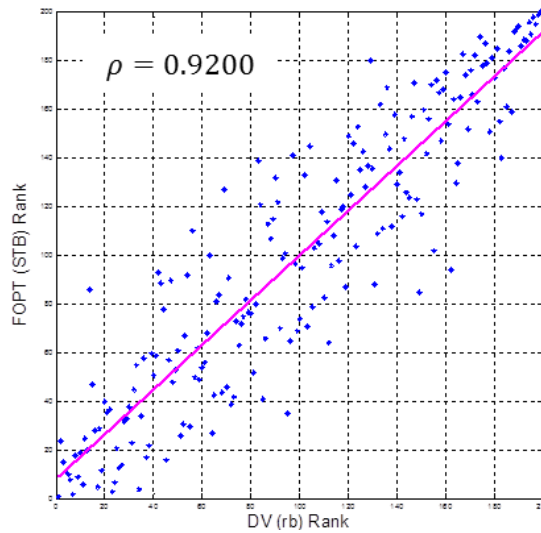


Figure 2.5: Rank correlation plot between DV and FOPT for the 2-D case

$$\mathcal{E}_{mean} = \sum_{i=1}^N \left[1 - \left(E[\zeta]_{est.} / E[\zeta]_{MC} \right) \right]^2 \quad (2.17)$$

$$\mathcal{E}_{std} = \sum_{i=1}^N \left[1 - \left(\sigma(\zeta)_{est.} / \sigma(\zeta)_{MC} \right) \right]^2 \quad (2.18)$$

Here $E(\zeta)|_{est.}$ and $\sigma(\zeta)|_{est.}$ respectively refer to the estimated mean and standard deviation while

$E(\zeta)|_{MC}$ and $\sigma(\zeta)|_{MC}$ refer to the true (Monte Carlo) mean and standard deviation respectively.

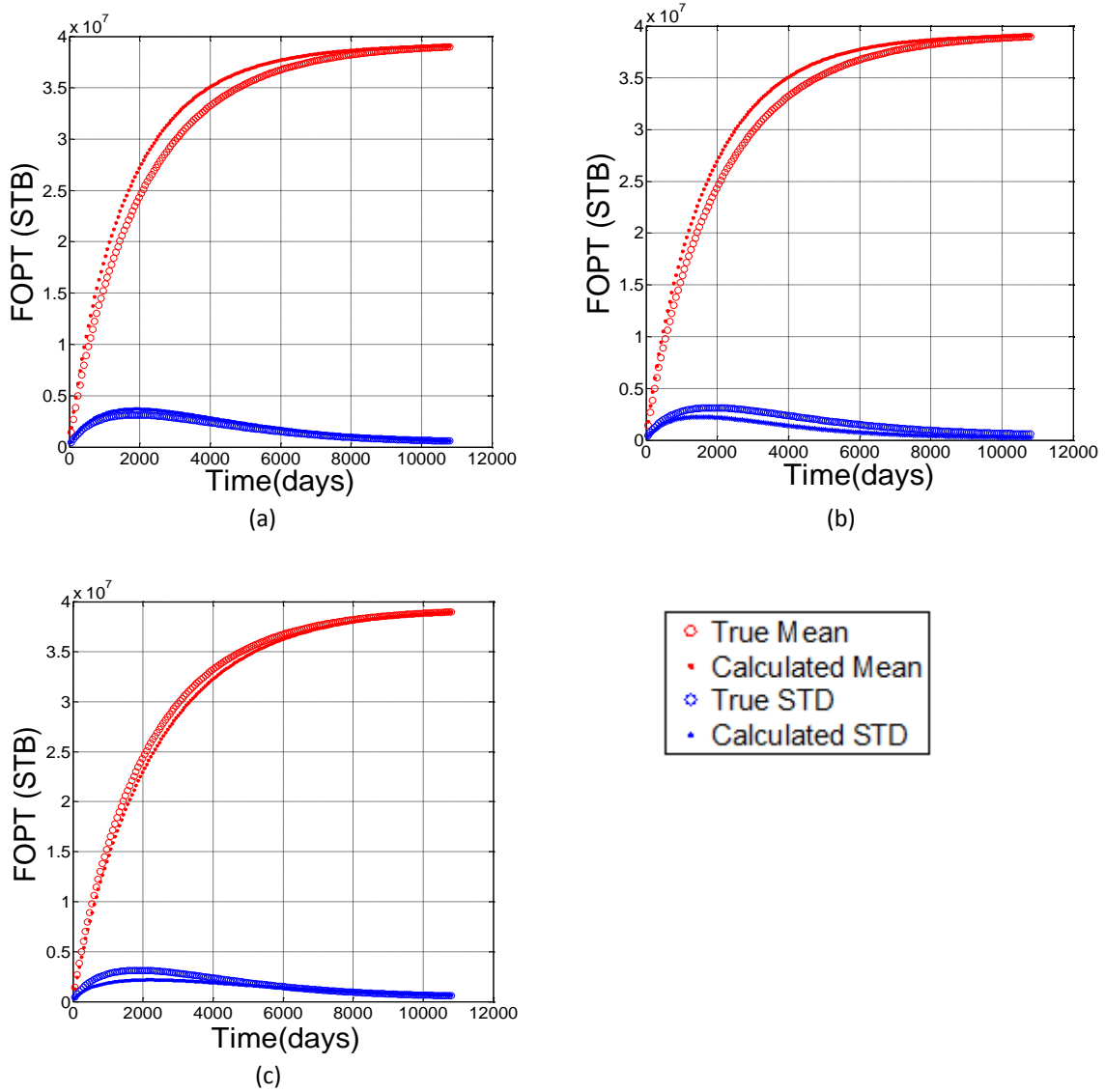


Figure 2.6: Cumulative oil production forecasts for the 2D case using (a) the P5-P50-P95 method, (b) the P10-P50-P90 method and (c) the Gaussian quadrature method

The results of the error calculations are displayed in **Table 2.1** which clearly reveals the superior forecast obtained with the Gaussian Quadrature method for the 2-D case. Also, the P5-P50-P95 method gave better results than the P10-P50-P90 method.

Table 2.1: Error quantification for the 2D Case

| | P5-P50-P95 | P10-P50-P90 | GAUSSIAN QUAD. |
|----------------------|------------|-------------|----------------|
| \mathcal{E}_{mean} | 1.4359 | 1.1171 | 0.2829 |
| \mathcal{E}_{std} | 6.1282 | 33.0077 | 6.4712 |

2.4 Illustration 2: A 3D Example

We applied the proposed ranking methodology to a 3D synthetic heterogeneous reservoir. An ensemble of 100 geostatistical realizations of both permeability and porosity were generated using Sequential Gaussian Simulation (Remy, 2005) using a synthetic well log data set. The reservoir was uniformly discretized into $85 \times 120 \times 11$ Cartesian grids, each with dimension $25 \times 25 \times 25$ ft. In addition to the assumptions made for the 2D case, gravity was ignored here.

Four identical, vertical and fully penetrating producers were placed in the single phase oil reservoir as shown in Fig. 2.7. The reservoir and well bottom hole pressure pressures were maintained similar to the 2-D case. Here also, the overall objective was to rank all models based on the field-wide cumulative production (FOPT) over a period of 15 years. The FMM was applied to calculate the drainage volumes of each model in the ensemble and a threshold pressure front arrival time of 25 days was applied on the drainage volume for the purpose of ranking the models. The choice of the cut-off time here is also based on the inception of interference similar to the 2-D case. To confirm the suitability of the drainage volume at the specified cut-off time, the rank correlation with the FOPT at the end of the depletion period was

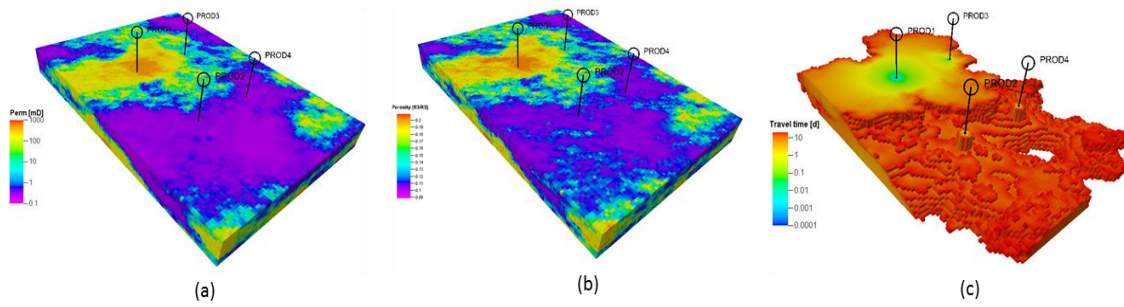


Figure 2.7: (a) Permeability, (b) Porosity and (c) Diffusive time of flight profiles for one 3D model

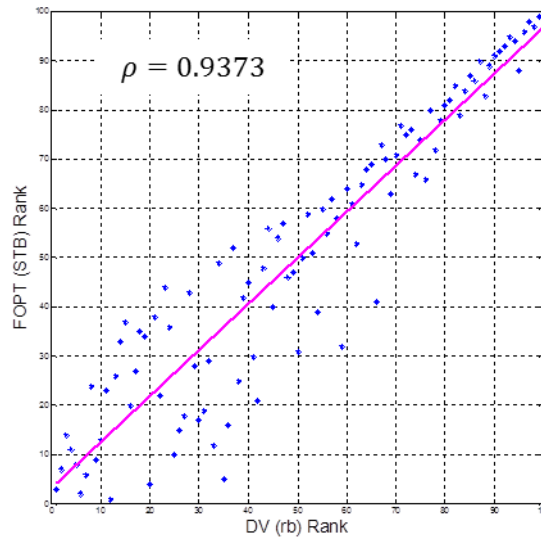


Figure 2.8: Rank correlation between DV and FOPT for the 3-D case

calculated to be 0.94 as shown in **Fig. 2.8**. This confirmed the suitability of the selected surrogate parameter. The models were ranked based on the drainage volume distribution and model selections made for full simulation using the methods discussed. Full simulation was run for all selected models using the ECLIPSE commercial reservoir simulator to obtain the FOPT up to a period of 15 years. Then uncertainties in FOPT were likewise calculated using the expressions in **Eqs. (2.15)** and **(2.16)**.

Forecast results obtained using the three model selection methods are compared with those from the Monte Carlo method as shown in **Fig. 2.9 (a)** through **(c)**. In each of the plots, the legends take the same form as for the 2-D case. As was done in the 2-D case, the errors between the estimated mean \mathcal{E}_{mean} and standard deviation \mathcal{E}_{std} and those obtained by Monte Carlo simulation were also quantified for each of the methods using **Eqs. (2.17)** and **(2.18)**. The results of this calculation are presented in **Table 2.2**. Again, from this table and from the plots, the superiority of the Gaussian Quadrature method of forecast is noticeable.

Table 2.2: Error quantification for the 3D Case

| | P5-P50-P95 | P10-P50-P90 | GAUSSIAN QUAD. |
|----------------------|------------|-------------|----------------|
| \mathcal{E}_{mean} | 3.9937 | 0.5667 | 0.1936 |
| \mathcal{E}_{std} | 69.6799 | 41.1586 | 5.0127 |

2.5 Discussion

The improved performance of the Gaussian quadrature method in both cases considered could be attributed to the inherent simultaneous model selection and weights calculation approach involved, which are constrained on the preservation of the first $2N - 1$ moments of the drainage volume distribution. It precludes the pre-determined choice of percentiles for model selection as in the P5-P50-P95 and P5-P50-P95 methods. The two traditional methods can, nevertheless be applied with reasonable accuracy in many instances. However it is still fuzzy to *a priori* choose one of the two traditional model selection methods to give the best forecast in any scenario.

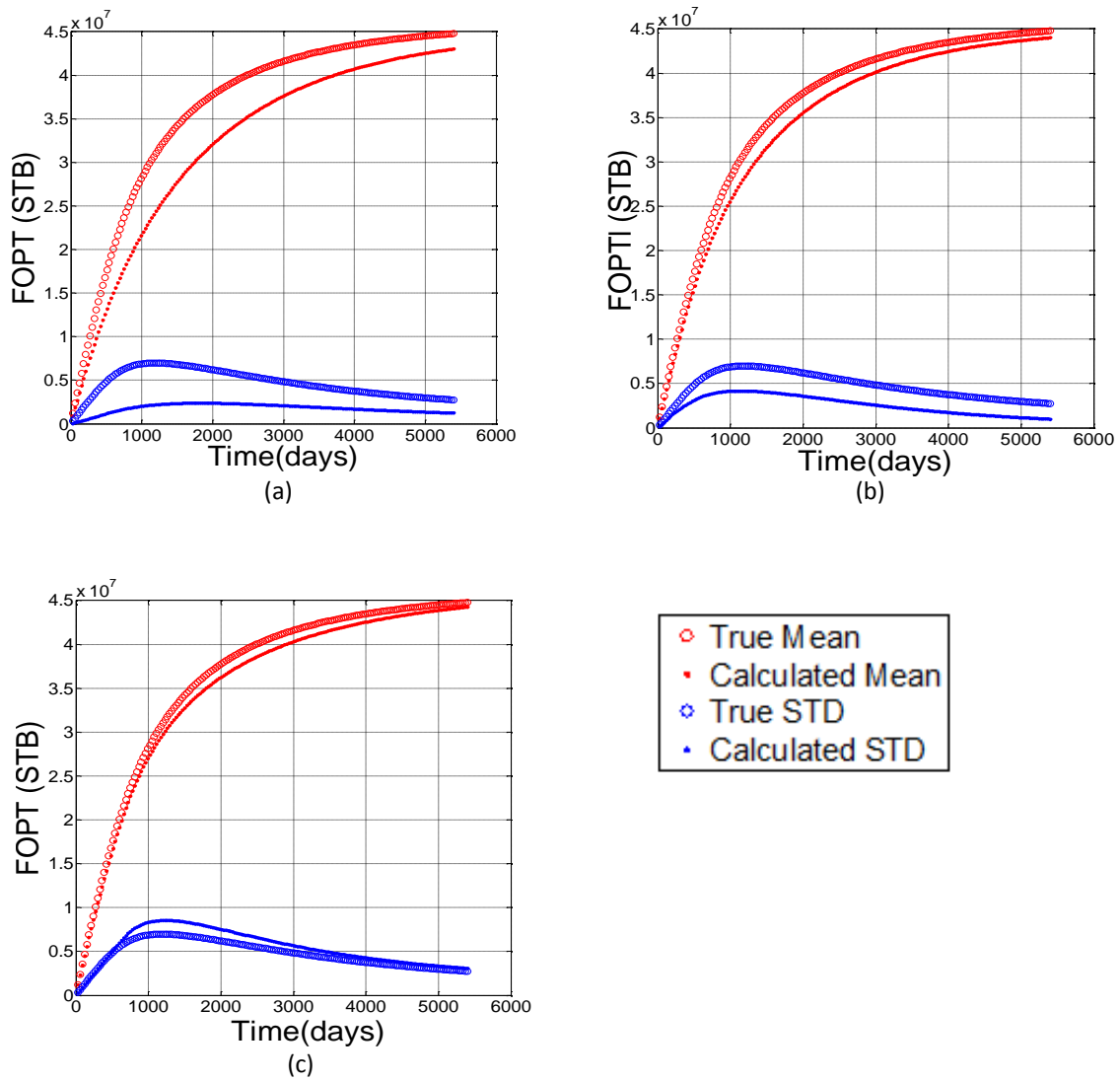


Figure 2.9: Cumulative oil production forecasts for the 3D cases using (a) the P5-P50-P95 method, (b) the P10-P50-P90 method and (c) the Gaussian quadrature method

Furthermore for the Gaussian quadrature method, there are no ground rules for deciding the number of point discretization N required to perform the uncertainty quantification. It was observed in this work that 3, 4 and 5 points discretization give good results. For values of 6 and above however, the system of equation solved often becomes ill-conditioned; a situation that will result in bad forecasts.

For both 2-D and 3-D cases, the uncertainty analysis has been summarized in **Fig. 2.10**. Here, we show the P10, P50 and P90 plots of the FOPT for the 2D and 3D cases. We also compare the performances of the model selection methods in predicting the true percentiles at few chosen time steps. In each case, and at every time steps desired, true percentiles were obtained by substituting the Monte Carlo mean $E(\zeta)|_{MC}$ and standard deviation $\sigma(\zeta)|_{MC}$ originally obtained into the inverse standard normal cumulative distribution function.

Since Gaussianity was assumed for the traditional model selection methods, the same procedure was followed in calculating the P10, P50 and P90 values of FOPT at each time step. Here however, the corresponding estimated mean $E(\zeta)|_{est.}$ and standard deviation $\sigma(\zeta)|_{est.}$ were applied in the calculation. For the Gaussian quadrature method, the estimated mean $E(\zeta)|_{est.}$ and standard deviation $\sigma(\zeta)|_{est.}$ as well as the estimates of the skewness $skew(\zeta)|_{est.}$ and kurtosis $kurt(\zeta)|_{est.}$ were included in the percentile evaluations. These extra parameters were estimated using the following equations:

$$skew(\zeta)|_{est.} = \frac{\sum_{i=1}^N \{P_i (\zeta(R_i) - E(\zeta)|_{est.})^3\}}{(\sigma(\zeta)|_{est.})^3} \quad (2.19)$$

$$kurt(\zeta)|_{est.} = \frac{\sum_{i=1}^N \{P_i (\zeta(R_i) - E(\zeta)|_{est.})^4\}}{(\sigma(\zeta)|_{est.})^4} \quad (2.20)$$

The superiority of the Gaussian quadrature approach can also be observed from **Fig. 2.10**. For both 2D and 3D cases, the percentiles obtained using the Gaussian quadrature method gave the closest match with true percentiles.

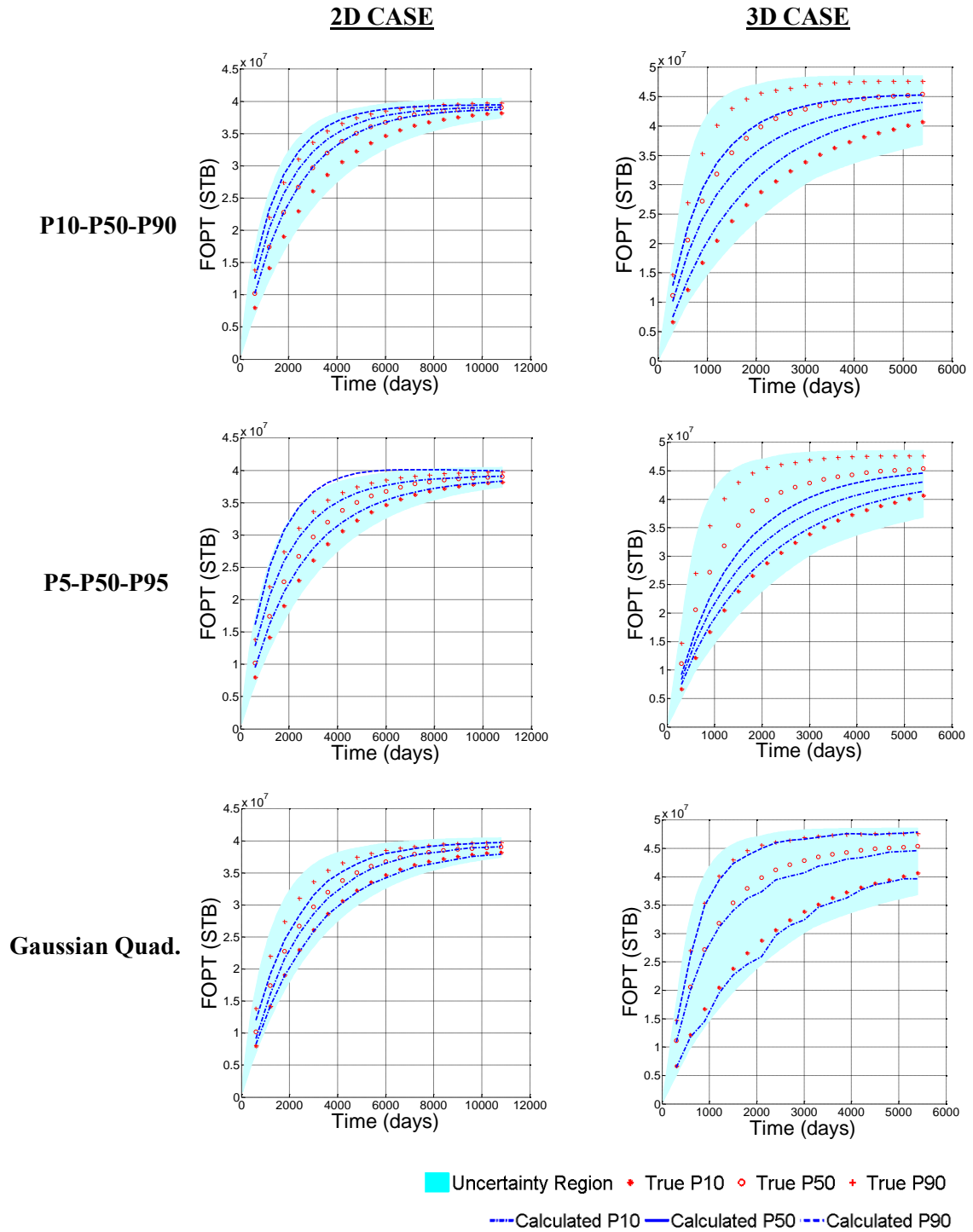


Figure 2.10: Uncertainty analysis plots

2.6 Summary

In this chapter, we have introduced a new rapid approach to ranking geologic models under primary depletion for uncertainty quantification using the drainage volume as the surrogate measure of the cumulative oil recovery (FOPT). The drainage volume of each model, as demonstrated for both 2D and 3D problems, can be quickly estimated using a class of front tracking algorithm known as the Fast Marching Methods (FMM). The constructed probability distribution functions (PDF) of the drainage volume can be point-discretized, allowing the selection of 3 models for full simulations to eventually construct the PDF of the FOPT.

Three model selection methods were also compared. It was shown that, due to its inherent capability of preserving higher order moments, the Gaussian quadrature method performs better than the traditional P5-P50-P95 and P10-P50-P90 approaches which may fail for non-Gaussian distributions.

CHAPTER III

RAPID TIGHT RESEVOIR MODEL CALIBRATION USING FAST MARCHING METHODS

In this chapter we focus on an important task in hydrocarbon reservoir management – reservoir model calibration, commonly known as history matching. The general idea is to integrate all available credible data and prior information into existing reservoir models so as to reduce the level of uncertainty and non-uniqueness in the models for improved and better refined forecasts. However, this process is inherently time consuming and computationally expensive especially for large reservoir models. It gets particularly difficult for unconventional and tight sands where simulation models are often set up with finer grids.

The goal in this chapter is to demonstrate the applicability of Fast Marching Methods (FMM) as a proxy in a two-stage Markov Chain Monte Carlo (MCMC) algorithm for multistage transverse hydraulic fracture models in unconventional oil reservoirs. We apply FMM to screen new models proposed in the search algorithm based on their responses. Due to the computational efficiency of FMM, unacceptable models are quickly screened out and valuable simulation time is saved. We also attempted to further exploit the speed of FMM in reservoir pressure field calculation. We applied FMM to obtain an estimate of the full field pressure profile and input this as an initial guess in matrix solvers. For the purpose of continuity however, the details of this are presented in Appendix A of this thesis.

3.1 Introduction

The World's unconventional resources are vast and current research work predicts more technically recoverable reserves than have been published hitherto (Dong et al., 2012; Holditch, 2006). More activities are therefore expected in the area of tight reservoir development for the next few decades (Holditch, 2006). This is made possible by advanced technologies in horizontal drilling and multistage transverse hydraulic fracturing. These hydraulic fractures serve as the major highway for fluid transport between the tight rock matrix to the well bore. In most cases, unconventional reservoirs contain natural fractures which tend to open up during hydraulic fracturing jobs, thereby creating very complex fracture networks. Of course, the step preceding any reservoir model calibration process is the development of a reasonably efficient and reliable forward model. However, creating accurate numerical models to represent these reservoir systems can be challenging and expensive.

Two major approaches that have been adopted for modeling such complex fractured systems are the Dual Porosity/Dual Permeability (DPDK) and the Discrete Fracture Network (DFN) approaches. Warren and Root (1963) introduced the Dual Porosity as the 'sugar cube model' for modeling single phase fractured reservoirs. This was extended by (Kazemi et al., 1976) for multiphase flow in fractured reservoirs. Hill and Thomas (1985) later came up with the more robust Dual Permeability concept which was able to handle finite conductivity fractures. Both the Dual Porosity (Du et al., 2010; Du et al., 2011) and the Dual Permeability (Novlesky et al., 2011) concepts have been popular choices for hydraulically fractured tight reservoirs. However these methods only give good solutions for a large number of highly connected small-scale fractures, as argued by Moinfar et al. (2011). The DFN approach, on the other hand has shown great promise in overcoming the downsides of the DPDK approach (Karimi-Fard et al., 2003;

Moinfar et al., 2012; Monteagudo and Firoozabadi, 2004). Attempts have also been made to create a hybrid of the two approaches (Johns et al., 2013). The DFN approach however quickly gets very complicated and computationally difficult as the scale of the problem increases, posing a great challenge for history matching.

In many cases today, history matching problems are based on simplified, yet realistic models which reasonably account for the flow complexities occurring in hydraulically fractured reservoir systems. One of such simplifications involves assuming that all flow is linear and perpendicular to the planar hydraulic fractures and does not extend beyond the tip of the fractures (Ambrose et al., 2011; Bello and Wattenbarger, 2010; Virieux et al., 1994). This allows modeling hydraulic fracture systems as high permeability planes within a box-shaped Simulated Reservoir Volume (SRV) with a constant induced permeability value. Gildin et al. (2013) later showed that a permeability distribution that varies linearly or exponentially with the distance from the hydraulic fracture better reproduces production data. These models and other variants have been a commonplace in tight reservoir forecasting approaches using pressure and rate transient analyses (Bello and Wattenbarger, 2010; Samandarli et al., 2011; Thompson et al., 2011). Analytical history matching approaches are, however, overly simplistic and may not be predictive by nature. Also, like other deterministic approaches, they do not provide range of uncertainties useful for prudent decision making.

Simple numerical models are now being applied to set up more realistic hydraulic fracture models which incorporate more flow physics and geomechanics for the purpose of less expensive history matching schemes (Cipolla et al., 2009). Uncertainties can also be accounted for and further reduced by integrating microseismic and production data into these models (Cipolla et al., 2010; Cipolla et al., 2011; Mayerhofer et al., 2006). Rigorously accounting for

uncertainties in history matching workflows typically requires probabilistic and/or heuristic approaches including data assimilation via Ensemble Kalman Filter (EnKF) approaches (Aanonsen et al., 2009), population based algorithms (Hajizadeh et al., 2010) which recently gained wide popularity and rigorous sampling algorithms such as the Markov Chain Monte Carlo (MCMC) (Hastings, 1970). The MCMC method, which is used to generate complex posterior distributions of calibrated models, requires several simulations; a lot of which may be rejected. For large or complex models such as hydraulic fracture systems the approach becomes impractical. To solve this problem, a two-stage MCMC algorithm was designed to screen model proposals in the first stage using a fast approximate simulator referred to as the proxy (Efendiev et al., 2005; Efendiev et al., 2006; Ma et al., 2008). The success of this algorithm, of course hinges on a consistent and reasonably accurate proxy.

A Fast Marching Method (FMM)-based proxy was recently applied by Yin et al. (2011) in a Genetic Algorithm (GA) approach to a synthetic shale gas model calibration problem. The non-uniqueness of the problem was reduced by constraining each proposed model's drainage volume, calculated using FMM (Xie, Gupta, et al., 2012), to the microseismic-data-defined drainage volume. The FMM has also been applied as a forward model to quickly estimate production response using the geometric pressure approximation method (Xie, Yang, et al., 2012). The validity of the forward FMM model was however not verified with more accurate conventional finite difference simulator results.

In this work, we demonstrate the applicability of the FMM geometric pressure approximation as a suitable proxy in a two-stage MCMC algorithm for integrating production data into a synthetic tight reservoir model. In this problem, hydraulic fractures were represented as elliptical planes, each surrounded by an induced ellipsoidal high permeability region (Ge and Ghassemi, 2011).

In the two-stage MCMC algorithm, model proposals were screened in the first stage using the FMM proxy based on their production responses. Only screened and potentially acceptable models proceed to the second stage where full simulations are carried out. Due to the speed of proxy evaluations, the two-stage MCMC was expected to be more efficient compared to the standard (single-stage) MCMC.

3.2 Methodology

In this section, we first provide the formulation of the geometric pressure approximation based on drainage volume estimated using FMM (Xie, Gupta, et al., 2012). This served as the proxy used to screen model proposals during the history matching process. Second, we pose the inverse problems formulation in the Bayesian framework. Here, the mathematical details guiding both the single stage MCMC and the two-stage MCMC algorithms will be described. Finally, we describe the history matching problem to which these concepts were applied.

3.2.1 Proxy Construction

The geometric pressure approximation formulation (Xie, Gupta, et al., 2012) starts from expressing the diffusivity equation given by:

$$\phi c_i \frac{\partial p}{\partial t} = \frac{1}{r} \left(\frac{\partial}{\partial r} \left(\frac{k}{\mu} r \frac{\partial p}{\partial r} \right) \right) \quad (3.1)$$

in terms of the Darcy flux Q given by:

$$Q = \frac{kA(r)}{\mu} \frac{\partial p}{\partial r} \quad (3.2)$$

Therefore **Eq. (3.1)** can be written as:

$$A(r)\phi c_t \frac{\partial p}{\partial t} = \frac{\partial Q}{\partial r} \quad (3.3)$$

where $A(r) = 2\pi rh$ refers to the curved surface area for cylindrical flow (with $r = \sqrt{x^2 + y^2}$) and $A(r) = 4\pi r^2$ refers to the curved surface area for spherical flow (with $r = \sqrt{x^2 + y^2 + z^2}$). The pore volume is also expressed in terms of the surface area $A(r)$:

$$V_p = \phi \int_0^r A(r) dr \quad (3.4)$$

And this is substituted into **Eq. (3.3)** to give:

$$c_t \frac{\partial p}{\partial t} = \frac{\partial Q}{\partial V_p} \quad (3.5)$$

For the geometric pressure approximation, the following assumptions are made:

- The Darcy flux is negligible outside the drainage volume, that is $Q = 0$ as $V_p \rightarrow V_p(r)$ and $Q = Q_w$ as $V_p \rightarrow 0$; and
- The steady state solution provides a good approximation of the pressure within the drainage volume, that is:

$$\bar{p} = \frac{1}{V_p(r)} \int_0^{V_p(r)} p dV_p \quad (3.6)$$

Applying the boundary conditions in the first assumption and substituting **Eq. (3.6)** into **Eq. (3.5)**, the following is obtained:

$$\frac{\partial p}{\partial t} \cong \frac{\partial \bar{p}}{\partial t} = -\frac{1}{c_t} \frac{Q_w}{V_p(r(t))} \quad (3.7)$$

Solving for pressure requires transforming from the diffusive time of flight $\tau(\mathbf{x})$ obtained from FMM to pressure front arrival time $t(\tau)$. In homogeneous flow media, the $\tau-t$ transformation is given simply as $\tau = \sqrt{\beta t}$; where $\beta = 2, 4$ and 6 for linear, radial and spherical flow regimes respectively (Ertekin et al., 2001). For cases like the hydraulic fractured reservoir systems where flow regimes continually change with time, the $\tau-t$ transformation takes the form (Zhang et al., 2013):

$$t(\tau) = \left(\int_0^\tau \frac{d\tau'}{\sqrt{\beta(\tau')}} \right)^2 \quad (3.8)$$

$$\text{where } \beta(\tau) = 2 \frac{\ln V_p(\tau)}{\ln \tau} \quad (3.9)$$

Plotting $\ln V_p(\tau)$ versus $\ln(\tau)$, it is easy to verify that **Eq. (3.8)** reduces to the $\tau-t$ transformation expression for the homogeneous cases. Finally, the bottom hole pressure (BHP) of a producer constrained at rate Q_w can be obtained:

$$p(0, t) \cong p_i - \frac{Q_w}{c_t} \int_0^t \frac{dt}{V_p(t)} \quad (3.10)$$

Pressure profile with respect to time and space of the entire reservoir due to rate constrained wells (producers or injectors) can also be estimated by applying **Eq. (3.10)** in a superposition approach. This method is presented in Appendix A of this thesis.

3.2.2 Bayesian Approach to Inverse Problems

In the Bayesian framework, inverse (history matching) problems are approached probabilistically. This technique relies mainly on the Bayes' theorem given as:

$$P(\mathbf{X} | \mathbf{d}_{obs}) \propto P(\mathbf{d}_{obs} | \mathbf{X})P(\mathbf{X}) \quad (3.11)$$

where $P(\mathbf{d}_{obs} | \mathbf{X})$ and $P(\mathbf{X})$ respectively represent the Likelihood and Prior probability distribution functions (PDF) while $P(\mathbf{X} | \mathbf{d}_{obs})$ is referred to as the posterior PDF. In reservoir model calibration problems, the idea is to update prior models \mathbf{X} distributed in the prior PDF using current data \mathbf{d}_{obs} such as well BHP or flow rate data, distributed in the Likelihood PDF to obtain the posterior PDF. Assuming the prior model and the data errors follow Gaussian distribution, then the posterior distribution can be expressed as (Oliver et al., 2008):

$$P(\mathbf{X} | \mathbf{d}_{obs}) \propto \exp\left[-\frac{1}{2}(\mathbf{d}_{sim} - \mathbf{d}_{obs})^T \mathbf{C}_D^{-1}(\mathbf{d}_{sim} - \mathbf{d}_{obs})\right] \exp\left[-\frac{1}{2}(\mathbf{X} - \mathbf{X}_{pr})^T \mathbf{C}_X^{-1}(\mathbf{X} - \mathbf{X}_{pr})\right] \quad (3.12)$$

Defining a measure of history match referred to as *misfit* given as:

$$misfit = (\mathbf{d}_{sim} - \mathbf{d}_{obs})^T \mathbf{C}_D^{-1}(\mathbf{d}_{sim} - \mathbf{d}_{obs}) + (\mathbf{X} - \mathbf{X}_{pr})^T \mathbf{C}_X^{-1}(\mathbf{X} - \mathbf{X}_{pr}) \quad (3.13)$$

Then

$$P(\mathbf{X} | \mathbf{d}_{obs}) \propto \exp\left[-\frac{1}{2}(misfit)\right] \quad (3.14)$$

where \mathbf{C}_D and \mathbf{C}_X respectively are the data and model parameter covariance matrices while \mathbf{d}_{sim} represents the calculated model response. The first term on the RHS of **Eq. (3.13)** is referred to as the Likelihood while the second term measures the deviation from the prior. For multi-dimensional problems as we have in reservoir history matching, the posterior PDF however gets

too complicated to estimate in closed form. Complicated PDFs like this are usually estimated using efficient sampling methods such as the Metropolis-Hastings Markov Chain Monte Carlo (MCMC) algorithm. This algorithm was designed to run an ergodic Markov chain through the parameter space and, with sufficiently long chain, eventually converge to a stationary distribution $P(\mathbf{X} | \mathbf{d}_{obs})$, describing the posterior PDF. The amount of time (iterations) it takes for the Markov chain to converge to a stationary distribution is referred to as the burn-in time n_{burn} . This approach helps to obtain an ensemble of reservoir models that are constrained to both data and prior information in a probability distribution, and therefore offers the advantage of accounting for uncertainties in history matching solutions.

The Single Stage MCMC Algorithm

This algorithm which was introduced by (Hastings, 1970) involves the following steps:

- At state \mathbf{X}_n , generate a propose a new state \mathbf{X} from a proposal distribution $q(\mathbf{X} | \mathbf{X}_n)$
- For the proposal \mathbf{X} , calculate the posterior probability $\pi(\mathbf{X})$ (given as the RHS of **Eq. (3.12)**). The likelihood term in $\pi(\mathbf{X})$ requires full-scale numerical simulation.
- Accept the proposal \mathbf{X} with probability:

$$\rho(\mathbf{X}_n, \mathbf{X}) = \min \left(1, \frac{q(\mathbf{X}_n | \mathbf{X})\pi(\mathbf{X})}{q(\mathbf{X} | \mathbf{X}_n)\pi(\mathbf{X}_n)} \right) \quad (3.15)$$

- Thus $\mathbf{X}_{n+1} = \mathbf{X}$ with probability $\rho(\mathbf{X}_n, \mathbf{X})$ and $\mathbf{X}_{n+1} = \mathbf{X}_n$ with probability $1 - \rho(\mathbf{X}_n, \mathbf{X})$.

In this problem, proposals are generated using the random walk sampler expressed as:

$$\mathbf{X} = \mathbf{X}_n + \delta\boldsymbol{\varepsilon} \quad (3.16)$$

where $\delta > 0$ refers to the step length and ε is a vector of random numbers sampled from a uniform distribution. It can be shown (Hastings, 1970) that for symmetric proposal distributions like was applied in this work, **Eq. (3.16)** reduces to:

$$\rho(\mathbf{X}_n, \mathbf{X}) = \min\left(1, \frac{\pi(\mathbf{X})}{\pi(\mathbf{X}_n)}\right) \quad (3.17)$$

These steps are usually repeated iteratively for sufficient $n > n_{burn}$ until sufficient samples are collected from the posterior distribution. This MCMC algorithm remains a powerful technique for sampling complicated posterior PDFs like those encountered in history matching problems. However, going by the typical acceptance rates (less than 30%), it becomes computationally prohibitive to implement this algorithm for large (many cell) reservoir models.

The Two-Stage MCMC Algorithm

To circumvent the inefficiency of the single stage MCMC method, the two stage MCMC algorithm was designed (Efendiev et al., 2005). In this approach, a fast model evaluator (proxy) is used to screen model proposals in the first stage. Based on its response, as determined by the proxy, a model proposal may either be rejected or proceed to the second stage where full simulations are run to evaluate the proposal. The algorithm involves the following steps:

- At state \mathbf{X}_n , generate a propose a new state \mathbf{X}' from a proposal distribution $q(\mathbf{X}' | \mathbf{X}_n)$
- Estimate the posterior probability $\pi^*(\mathbf{X}') = P(\mathbf{X}' | \mathbf{d}_{obs})$ of the proposal \mathbf{X}' . Here the FMM proxy model is used for the likelihood calculation.
- Calculate first stage acceptance probability:

$$\rho_1(\mathbf{X}_n, \mathbf{X}') = \min\left(1, \frac{q(\mathbf{X}_n | \mathbf{X}')\pi^*(\mathbf{X}')}{q(\mathbf{X}' | \mathbf{X}_n)\pi^*(\mathbf{X}_n)}\right) = \min\left(1, \frac{\pi^*(\mathbf{X}')}{\pi^*(\mathbf{X}_n)}\right) \quad (3.18)$$

- Thus $\mathbf{X} = \mathbf{X}'$ with probability $\rho_1(\mathbf{X}_n, \mathbf{X}')$ and $\mathbf{X} = \mathbf{X}_n$ with probability $1 - \rho_1(\mathbf{X}_n, \mathbf{X}')$
- If accepted, calculate the posterior probability $\pi(\mathbf{X})$ of the proposal \mathbf{X} . At this stage, a numerical simulator is used for computing the likelihood.
- Calculate second stage acceptance probability:

$$\rho_2(\mathbf{X}_n, \mathbf{X}) = \min\left(1, \frac{Q(\mathbf{X}_n | \mathbf{X})\pi(\mathbf{X})}{Q(\mathbf{X} | \mathbf{X}_n)\pi(\mathbf{X}_n)}\right) \quad (3.19)$$

where the instrumental distribution $Q(\mathbf{X} | \mathbf{X}_n)$ is given by:

$$Q(\mathbf{X} | \mathbf{X}_n) = \rho_1(\mathbf{X}_n, \mathbf{X}')q(\mathbf{X} | \mathbf{X}_n) + \left(1 - \int \rho_1(\mathbf{X}_n, \mathbf{X}')q(\mathbf{X} | \mathbf{X}_n)d\mathbf{X}\right)\delta_{\mathbf{X}_n}(\mathbf{X}) \quad (3.20)$$

- Finally $\mathbf{X}_{n+1} = \mathbf{X}$ with probability $\rho_2(\mathbf{X}_n, \mathbf{X})$ and $\mathbf{X}_{n+1} = \mathbf{X}_n$ with probability $1 - \rho_2(\mathbf{X}_n, \mathbf{X})$

In the above algorithm, if the trial proposal \mathbf{X}' is rejected in the first stage, then no full-scale simulation is required. If it is otherwise accepted, **Eq. (3.20)** represents the proposal distribution from which \mathbf{X} is effectively sampled from. Computing $Q(\mathbf{X} | \mathbf{X}_n)$ and $Q(\mathbf{X}_n | \mathbf{X})$ by the integral equation of Eq. (3.20) is however not required in this algorithm as it has been shown (Efendiev et al., 2005; Ma et al., 2008) that **Eq. (3.19)** naturally reduces to:

$$\rho_2(\mathbf{X}_n, \mathbf{X}) = \min\left(1, \frac{\pi^*(\mathbf{X}_n)\pi(\mathbf{X})}{\pi^*(\mathbf{X})\pi(\mathbf{X}_n)}\right) \quad (3.21)$$

In essence, the first stage only serves as a filter to avoid full (and costly) simulations for poor proposals. The comparative performances and efficiencies of both single and two stage MCMC

algorithms were evaluated using the final acceptance rates. The acceptance rate was simply defined as the *ratio of the new accepted proposals to the total number of proposals* of the Markov Chains in both algorithms. Also we adopted the maximum entropy criterion in the convergence diagnostics of each Markov chain. The entropy measure \mathbf{S} is calculated as the expectation value of the logarithm of un-normalized posterior values $\pi(\mathbf{X})$ mathematically expressed as (Maucec et al., 2007):

$$-\mathbf{S} = \int \pi(\mathbf{X}) \log \pi(\mathbf{X}) d\mathbf{X} \approx \langle \log \pi(\mathbf{X}) \rangle \quad (3.22)$$

From Eq. (3.22), the entropy \mathbf{S} of the posterior distribution is approximated using a Monte Carlo integration. A high and relatively stable value of the negative entropy calculated in Eq. (3.22) signifies a convergence of the Markov chain to a stationary distribution.

3.2.3 Problem Description

Here, we illustrate the application of these concepts with a synthetic hydraulic fractured reservoir model calibration. We considered a tight oil reservoir discretized into $150 \times 150 \times 11$ square grid cells, each 10ft in dimension. The reservoir was developed with a horizontal well with four-stage transverse hydraulic fractures equally spaced 250ft apart as shown in **Fig. 3.1**.

Model Assumptions

Regarding the model construction, the following simplifying assumptions were made:

Hydraulic fractures can be effectively modeled for reservoir simulation with transverse high permeability symmetric elliptical planes as shown in **Fig. 3.1 (a)**. The hydraulic fracture

- half-length x_f is given by half of the entire major axis length of the ellipse, while the height $2h_f$ is given by the entire length measured along its minor axis as labeled in **Fig. 3.1 (b)**.
- The local stimulated rock volume around a fracture stage may be represented by an ellipsoidal Enhanced Permeability Area (EPA) (Ge and Ghassemi, 2011) as shown in **Fig. 3.1 (c)**. This can be a reasonable assumption for hydraulic fracture models especially in the absence of microseismic and/or reliable fracture density data (Du et al., 2011). Essentially for this problem, each fracture stage was modeled as a single elliptical fracture plane at the center of an ellipsoidal EPA.
- All fracture permeabilities k_f , enhanced permeabilities k_e are similar for all fracture stages. Also the rock matrix is homogeneous in terms of permeability k_m and porosity ϕ .
- Lastly, reservoir fluid is single phase oil. Also, pressure effects on permeability are negligible.

History Matching Problem Set-up

We considered updating the prior hydraulic fracture model using the well bottomhole pressure (BHP) data. The horizontal well was assumed to have produced oil at a constant rate $Q_w = 100\text{BBL}/D$ for 360 days. **Fig. 3.2 (a)** shows the (target) reference model whose response is shown in **figure 3.2 (c)** as the observed data plotted together with the response of the base model shown in **Fig. 3.2 (b)**. The idea here is to perform a probabilistic search for all models that give minimum misfit between their respective responses and the observed data. In other words, we attempt to reduce the uncertainties in the reservoir model parameters in order to improve the predictive capacity of the updated models.

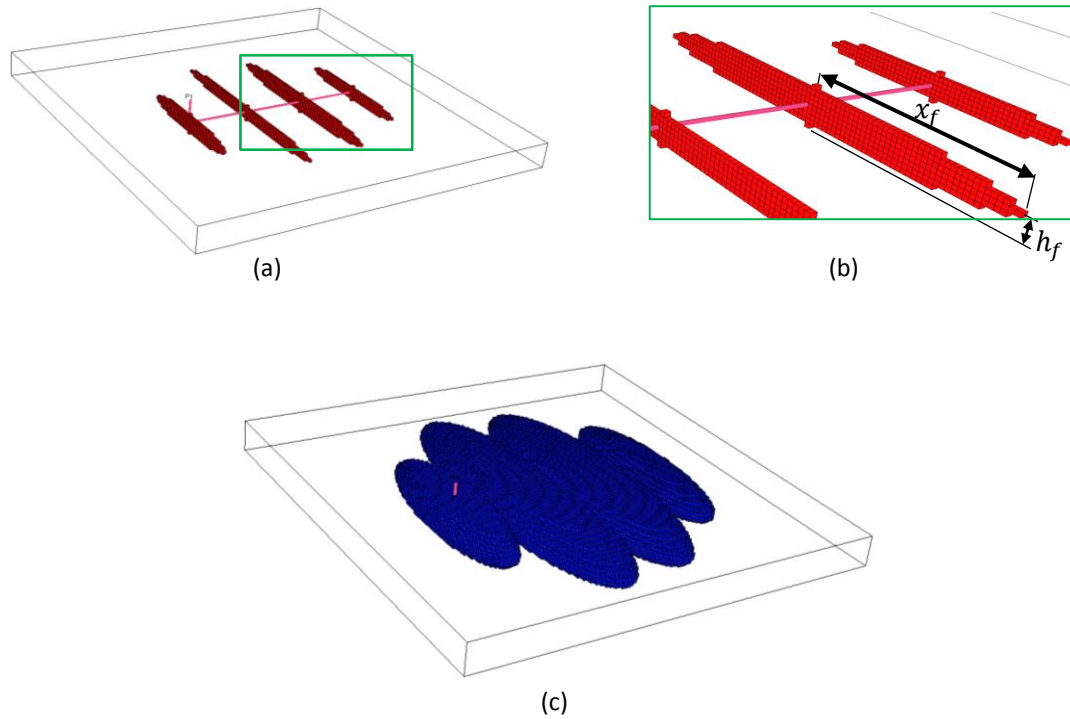
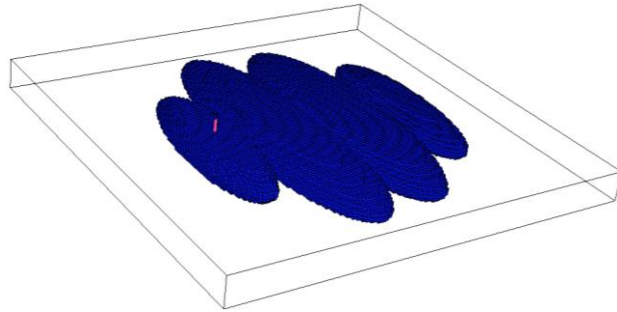


Figure 3.1: Hydraulic fracture model description showing (a) hydraulic fracture model with (b) an expanded view and (c) Enhanced Permeability Area (EPA)

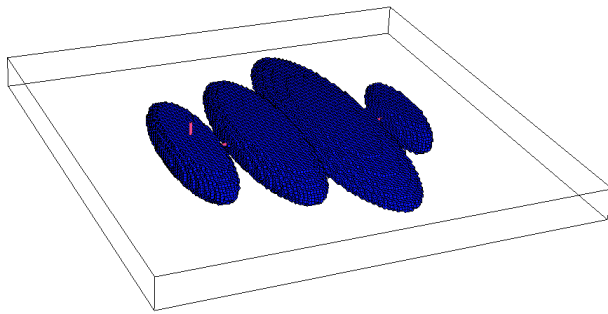
Model Parameterization

Table 3.1 shows the list of parameters used in the history matching problem. For each parameter, the reference, high, low and base values are also presented. Parameters describing the dimensions of the ellipsoidal EPA's are assumed to be directly related to the fracture dimensions. The ellipsoid major axis length a (along fracture main axis), minor axis length b (perpendicular to fracture plane) and the third axis length c (along the vertical direction) were expressed in terms of the fracture parameters as follows:

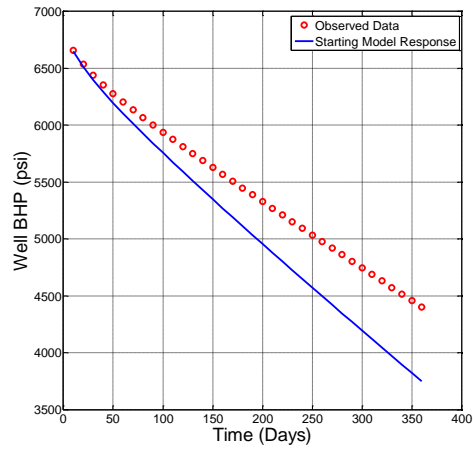
$$c = 2h_f; \quad b = 0.4x_f; \quad a = x_f + b \quad (3.23)$$



(a)



(b)



(c)

Figure 3.2: History matching problem set-up showing (a) the reference model, (b) the starting (base) model and (c) the simulated responses of both models

Table 3.1: List of model parameters

| PARAMETERS | REFERENCE | HIGH | LOW | BASE |
|--|----------------------|----------------------|---------------------|----------------------|
| Matrix Permeability, k_m (mD) | 100×10^{-6} | 150×10^{-6} | 70×10^{-6} | 145×10^{-6} |
| Enhanced Permeability, k_e (mD) | 0.017 | 0.025 | 0.005 | 0.023 |
| Fracture Permeability, k_f (mD) | 220 | 400 | 100 | 175 |
| Fracture 1 Half Length, x_{f_1} (ft) | 250 | 400 | 130 | 230 |
| Fracture 2 Half Length, x_{f_2} (ft) | 430 | 600 | 260 | 300 |
| Fracture 3 Half Length, x_{f_3} (ft) | 400 | 600 | 260 | 400 |
| Fracture 4 Half Length, x_{f_4} (ft) | 260 | 400 | 130 | 150 |
| Fracture 1 Half Height, h_{f_1} (ft) | 40 | 50 | 20 | 40 |
| Fracture 2 Half Height, h_{f_2} (ft) | 30 | 50 | 20 | 40 |
| Fracture 3 Half Height, h_{f_3} (ft) | 40 | 50 | 20 | 30 |
| Fracture 4 Half Height, h_{f_4} (ft) | 30 | 40 | 10 | 40 |

History Matching Algorithm Implementation

Both the single stage and two stage MCMC algorithms were implemented as described in the previous section. **Fig. 3.3** shows a diagrammatic representation of the two stage algorithm. In the first stage, trial proposals are evaluated by estimating the response $\mathbf{d}_{sim} = \mathbf{d}_{FMM}$ using the FMM-based geometric pressure approximation proxy as described earlier. As shown in **Fig. 3.4**, proxy approximations of the BHP response do not deviate significantly from simulation responses for the reference and both extreme cases. This demonstrates the suitability of the FMM geometric pressure approximation as a good proxy for this problem.

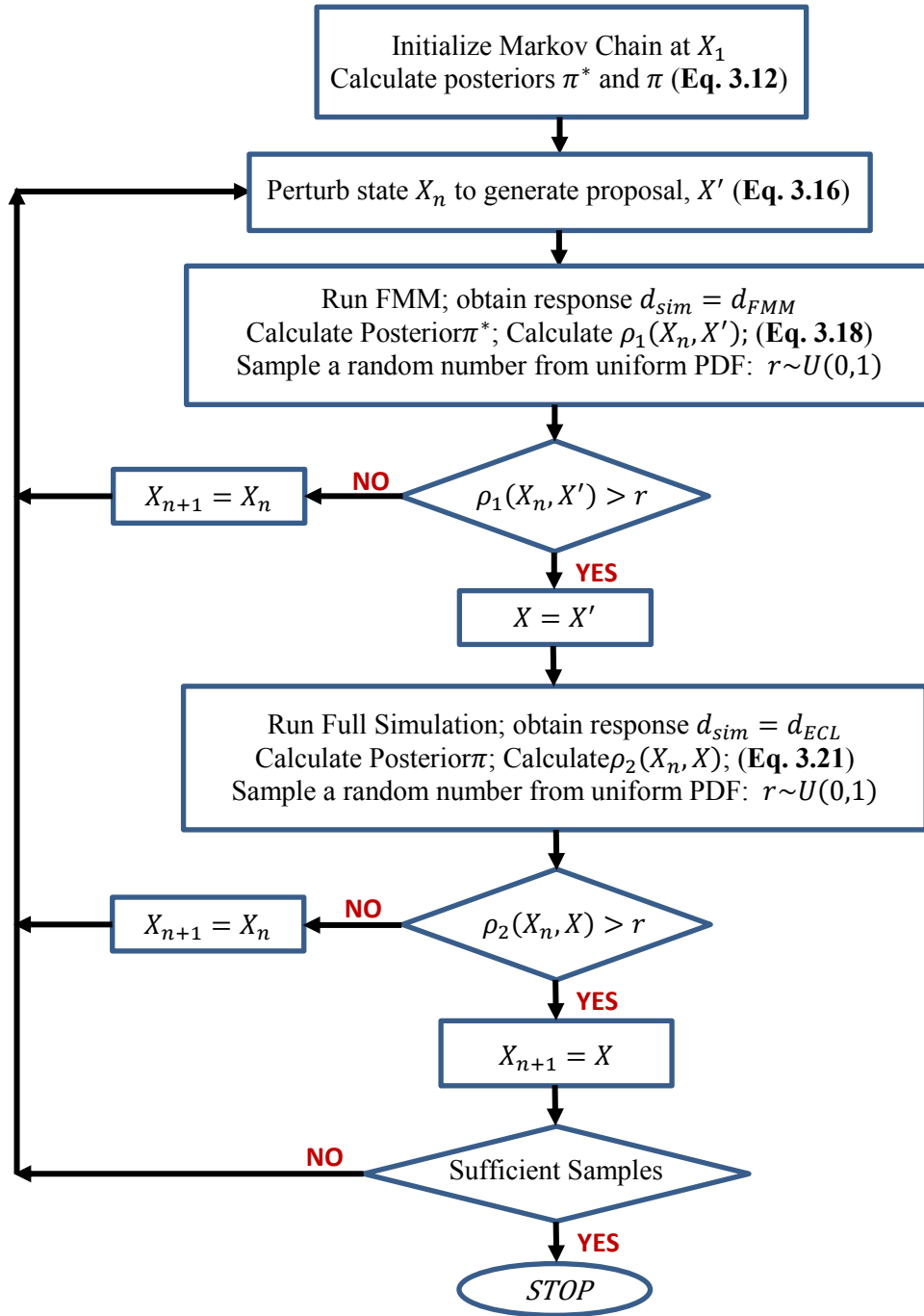


Figure 3.3: The two-stage MCMC algorithm flow chart

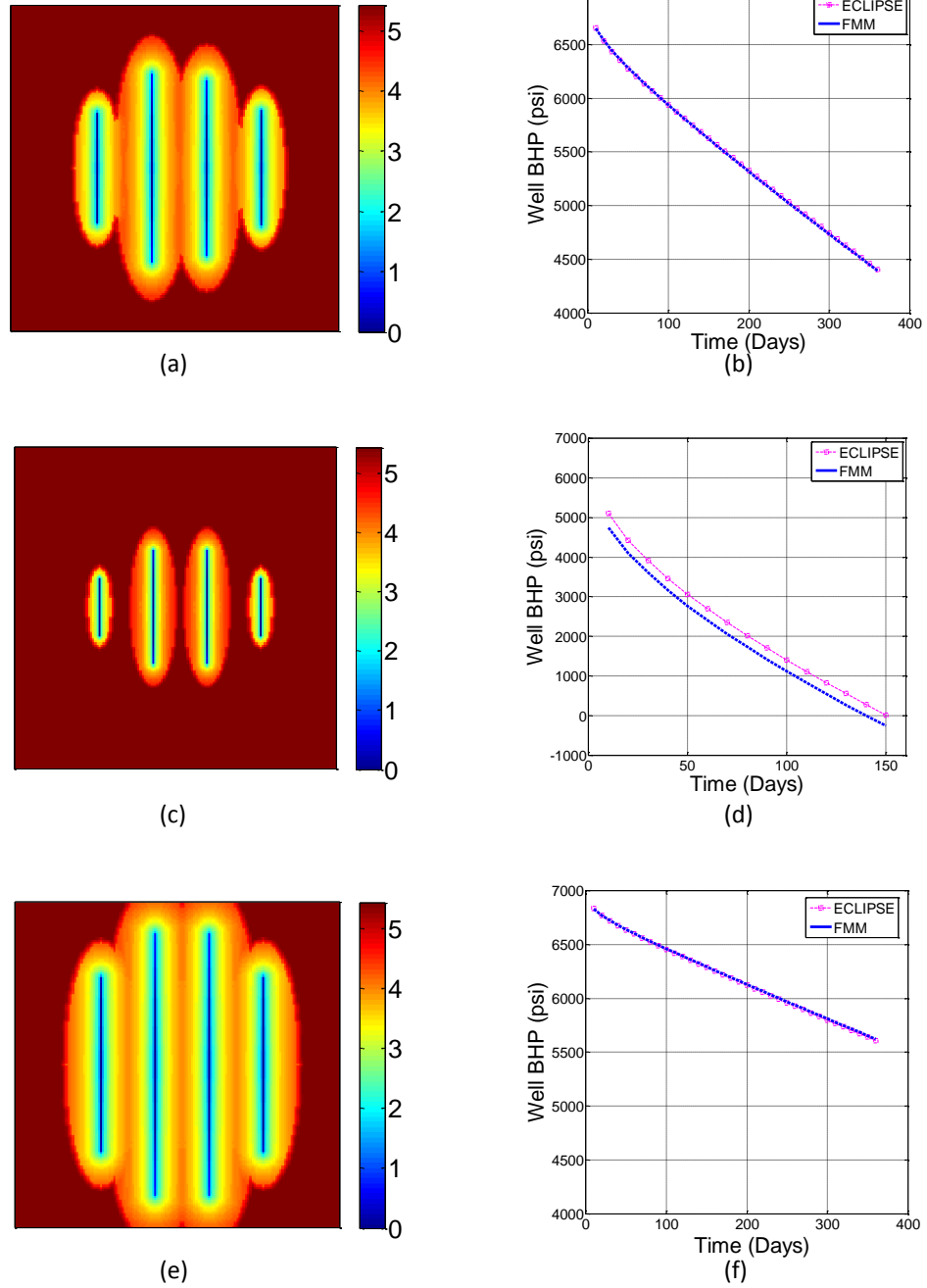


Figure 3.4: Logarithm of $\tau(\mathbf{x})$ contours and cross plots comparing pressure calculations between proxy and finite difference for the reference model [(a) and (b)], the lower extreme model [(c) and (d)] and the higher extreme model [(e) and (f)]

After first stage evaluations, all trial models are passed to the second stage and only proposals accepted in the first stage are evaluated with full simulations. All simulations in the second stage for this problem were carried out using the ECLIPSE[®] commercial software to obtain the model responses $\mathbf{d}_{sim} = \mathbf{d}_{ECL}$. The following were assumed for the terms required for the posterior calculation:

- Data (white) noise is assumed to be uncorrelated so that \mathbf{C}_D could be represented by a diagonal matrix. For this problem $\mathbf{C}_D = 2000\mathbf{I} \text{ psi}^2$, where \mathbf{I} is an identity matrix.
- All 11 parameters are uncorrelated so that \mathbf{C}_X is a diagonal matrix with each diagonal element defined by one-sixth of the range of corresponding parameter. \mathbf{X}_{pr} was defined by the arithmetic average of the high and low values of the parameters.

3.3 Results and Discussion

In this section, history matching results using the single stage MCMC algorithm will be presented first; then the results obtained using the two-stage MCMC algorithm will be presented.

Single Stage MCMC Results

The single stage MCMC algorithm was run over 1500 iterations, (requiring 1500 full simulations). The value of the calculated misfit at each state of the Markov chain is plotted in **Fig. 3.5 (a)**. Also the acceptance rate at each state is plotted in **Fig. 3.5 (b)**. As can be observed from these figures, the burn-in period for this Markov chain took 500 iterations. In other words, 500 full simulations were required for the chain to converge to a stationary distribution, after which the chain begins to sample from the desired posterior distribution. The overall acceptance rate for this chain settled at 12%, which means that 88% of the simulations were wasted.

The quality of the history match is pictorially presented in **Fig. 3.6**. Responses of 100 models randomly sampled within the range of uncertainty in the prior distribution are plotted in **Fig. 3.6(a)**. Also 100 calibrated model responses, sampled from the posterior distribution by the Markov chain after the burn-in time, are plotted in **Fig. 3.6 (b)**. In both plots, BHP responses were plotted to cover both the history period of 360 days (plotted in green) and the forecast period of another 360 days (plotted in blue). It is easy to see that the calibrated models provide excellent matches of the history. At the same time good prediction of future field performance.

Parameter uncertainty plots (boxplots) of prior and calibrated models are also shown in **Fig. 3.6 (c)** and **(d)** respectively. In these plots, each parameter value was normalized by the range of that parameter. The interval between the whiskers of each boxplot represents the entire range of uncertainty for the parameter represented. The upper and lower edges of each box represent the 75th and 25th percentiles respectively of the conditional distribution of each parameter.

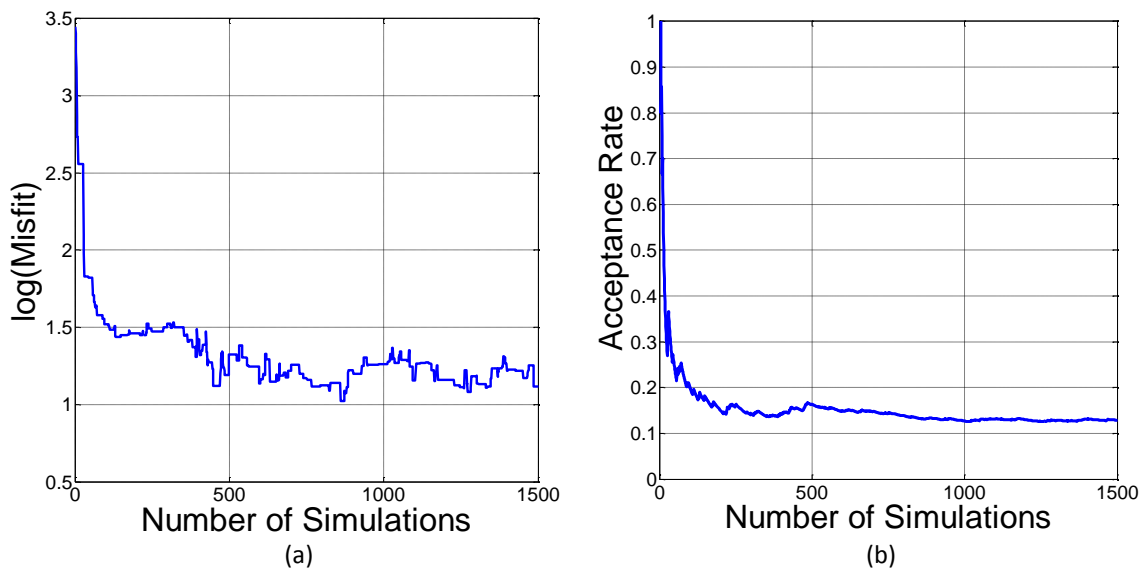


Figure 3.5: Single stage MCMC performance showing plots of the (a) misfit and (b) acceptance rate with iterations

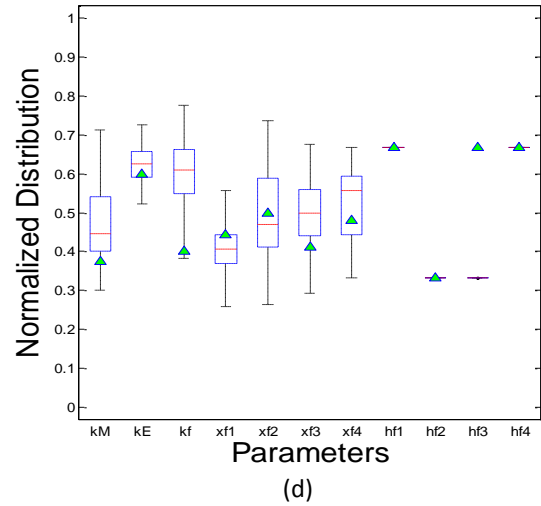
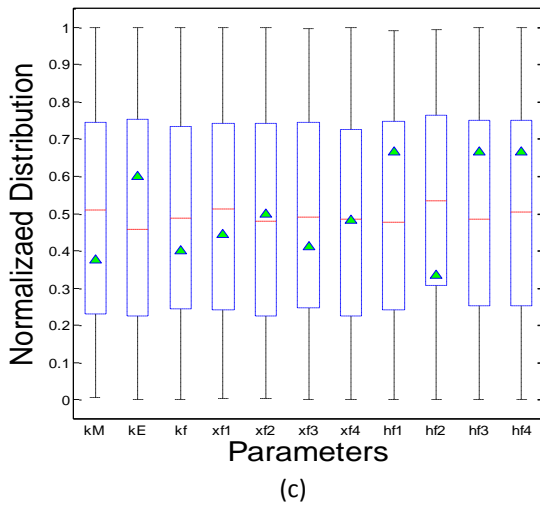
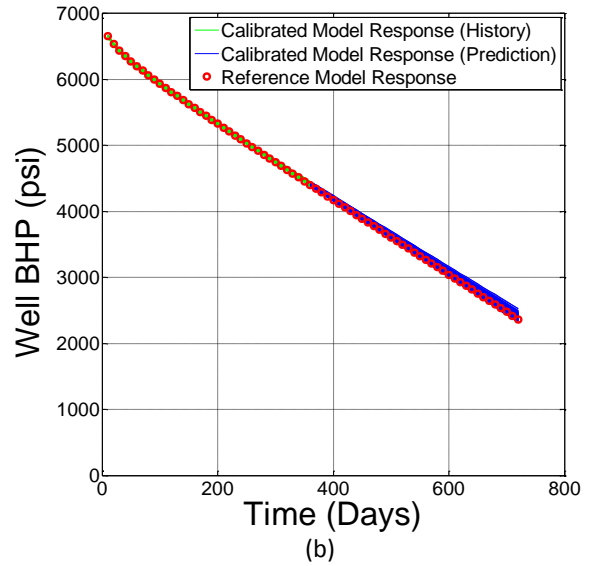
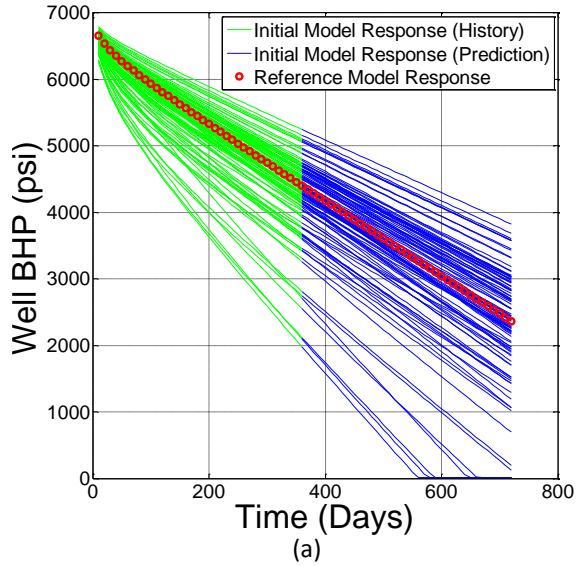


Figure 3.6: History matching results using the single stage MCMC algorithm showing (a) initial spread in responses, (b) final spread in responses, and boxplots depicting (c) initial parameter uncertainty and (d) final parameter uncertainty

The middle red lines are the respective medians of each parameter distribution while the green triangles represent the reference model parameters. The history matching method effectively reduces the parameter uncertainties as shown in **Fig. 3.6 (d)** compared with the prior uncertainties shown in **Fig. 3.6 (c)**. Also, the median values of each calibrated model parameter distribution closely matched the respective reference parameter values except for the matrix permeability k_M and fracture permeability k_f . Poor approximation of the k_M distribution can be attributed to its extremely low value which prevents sufficient propagation of the pressure front into the matrix within the historical period. On the other hand, a reason for the poor approximation of the k_f distribution is the typically high values of k_f , implying negligible pressure drop within fractures so that multiple k_f values could match historical data.

Regarding the efficiency of the single stage MCMC algorithm, each full simulation took 80 seconds on the average and therefore, about 31 hours was required for the Markov chain to both converge to the desired period distribution and to thereafter sample at least 100 models from the distribution. The two-stage MCMC algorithm was implemented to reduce the time required and therefore, to improve the overall efficiency of the history matching process.

Two-Stage MCMC Results

As shown in **Fig. 3.7 (a)** only a total 500 full simulations needed to be run in the two-stage MCMC since bad proposals are mostly “filtered” off using the FMM-based proxy. Also the burn-in period took less than 200 iterations after which more 160 models were sampled from the posterior distribution out of which the last 100 samples were extracted for uncertainty analysis.

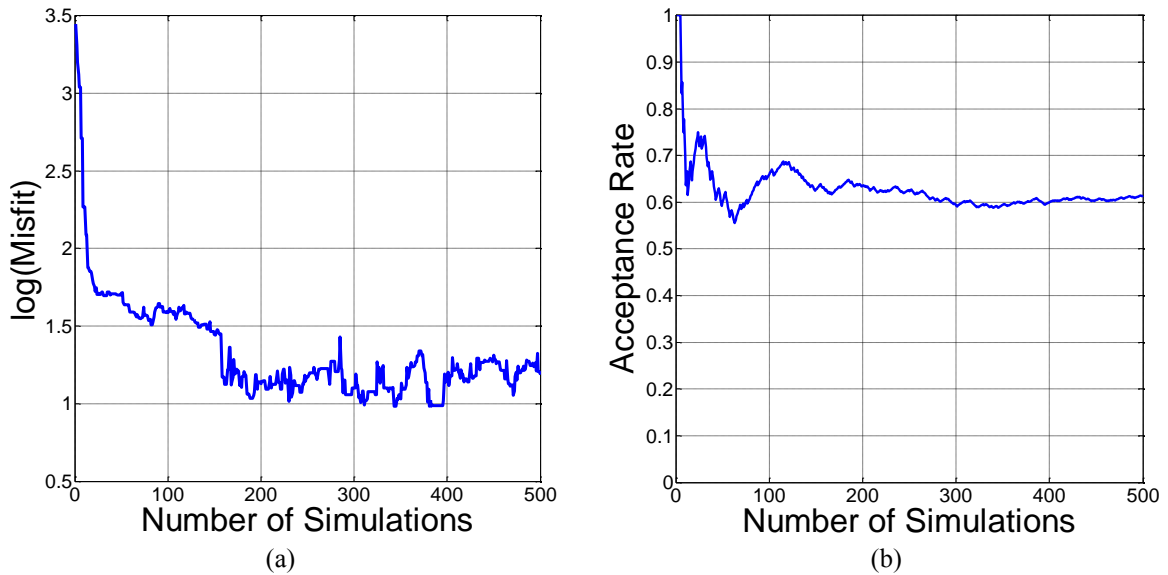


Figure 3.7: Two-stage MCMC performance showing plots of the (a) misfit and (b) acceptance rate with iterations

As shown in **Fig. 3.7 (b)** the acceptance rate for this algorithm settled at over 60% which is about 5 times what was obtained with the single stage MCMC algorithm. It is worthy of note here that these plots only show the misfits and acceptance rates versus the number of required full simulations. Unlike in the single stage algorithm, number of MCMC iterations here is more than the number of simulations.

Here likewise, the quality of the history match using the two-stage MCMC algorithm was studied. The graphic details of the uncertainty analysis are shown in **Fig. 3.8**. Color coding and graphical symbols in these plots have similar meaning as in the plots for the single stage MCMC results. From **Fig. 3.8 (b)**, it is clear that the two stage MCMC method sampled credible models that gave equally excellent matches with historical data and also made accurate predictions of

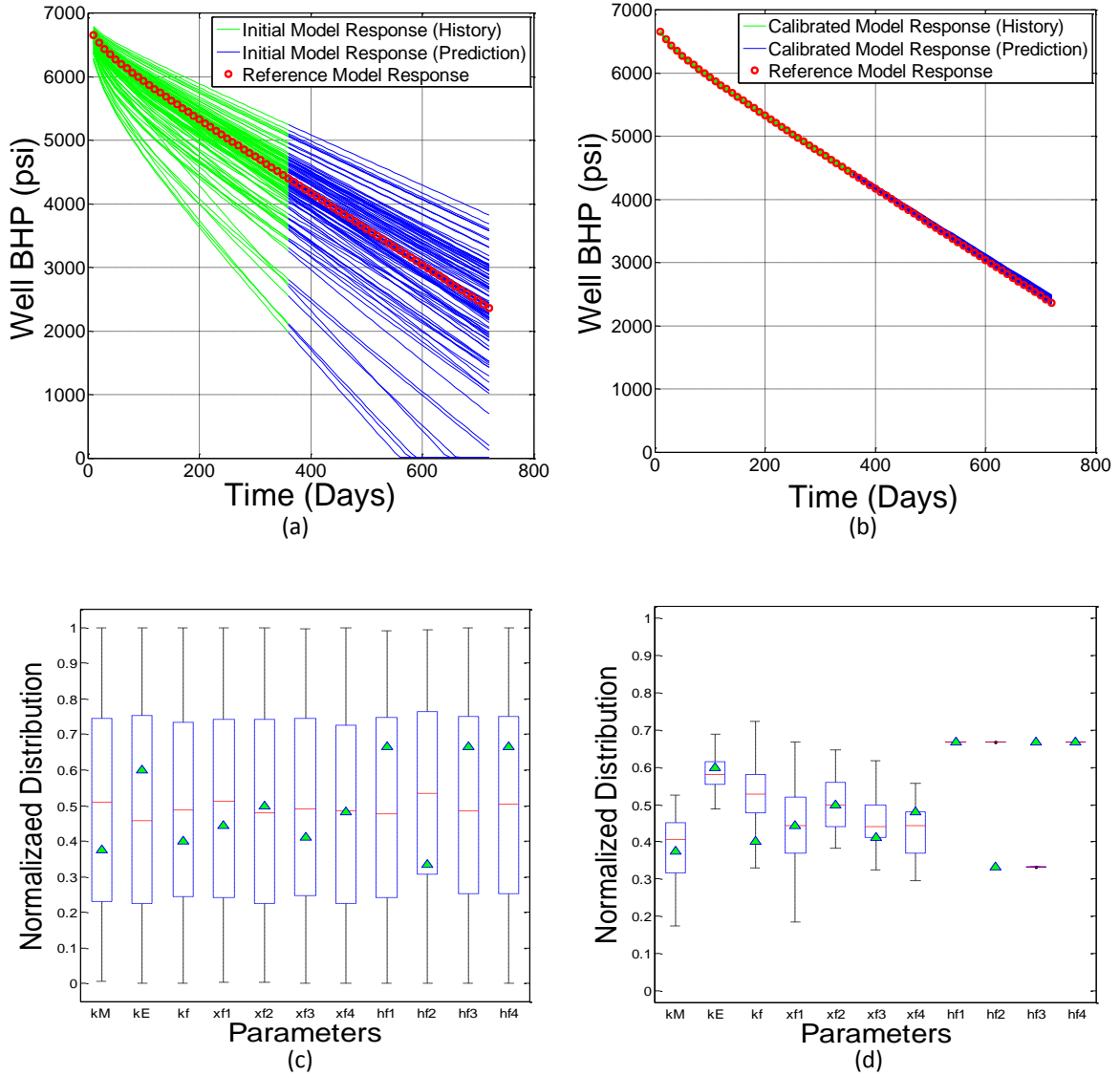


Figure 3.8: History matching results using the two-stage MCMC algorithm showing (a) initial spread in responses, (b) final spread in responses, and boxplots depicting (c) initial parameter uncertainty and (d) final parameter uncertainty

future reservoir performance. Considering the parameter boxplots in **Fig. 3.8 (c) and (d)**, parameter uncertainties were also drastically reduced like the single stage MCMC. The two- The two-stage MCMC however seemed to have better approximated each parameter's conditional distribution based on the closeness of the median of each distribution to the respective reference model parameters. This may be explained by the much higher acceptance rate in the two-stage MCMC (a consequence of a sufficiently accurate proxy) which allowed more samples to be drawn from the posterior distribution even with less number of full scale simulations.

Therefore, using the two-stage MCMC algorithm we were able to much more efficiently draw more samples from the posterior distribution. The FMM-based proxy evaluated each model within 2 seconds while full simulations required about 80 seconds on the average. Overall the total time required for the history matching using the two stage MCMC algorithm was less than 12 hours, implying almost *3 times* speed up of the history matching process compared to the single stage MCMC algorithm.

In this work, both single stage and two-stage MCMC algorithms were analyzed for convergence using the entropy plots. The entropy measure in the MCMC context is a measure of 'disorderliness' of the posterior function of the sampled models. In other words, the closer to zero the entropy measure of a Markov chain is, the clearer the indication that it has converged to a stationary distribution. The entropy measure, as calculated using **Eq. 3.22**, for both the single stage and two-stage Markov chains is plotted in **Fig. 3.9**. Here, the entropy measure is plotted against the number of iterations and not the number of simulations. The two-stage MCMC algorithm shows initial lower convergence rate depicted by the smaller entropy measure compared to that of the single-stage MCMC algorithm, but this difference attenuates as the number of iterations increases. The collapse of both plots at later iterations confirms the

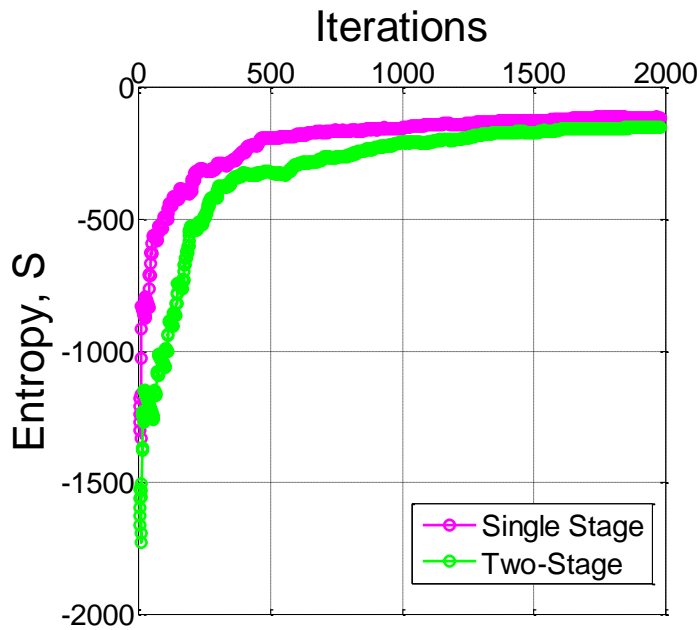


Figure 3.9: Entropy plots

consistency between the single stage and two-stage MCMC algorithms since they both sample from similar posterior distribution. The overall conclusion regarding the comparative efficiencies of both algorithms in this problem is that the acceptance rate is increased without substantial drop in convergence rate.

Finally, in **Fig. 3.10** we present the results of the history match in graphic detail. The non-uniqueness of the history match can be observed from the four models sampled from the posterior distribution. Integrating more data such as the temperature and production logging data can help dampen the non-uniqueness of the problem and also further reduce the uncertainty in the reservoir model.

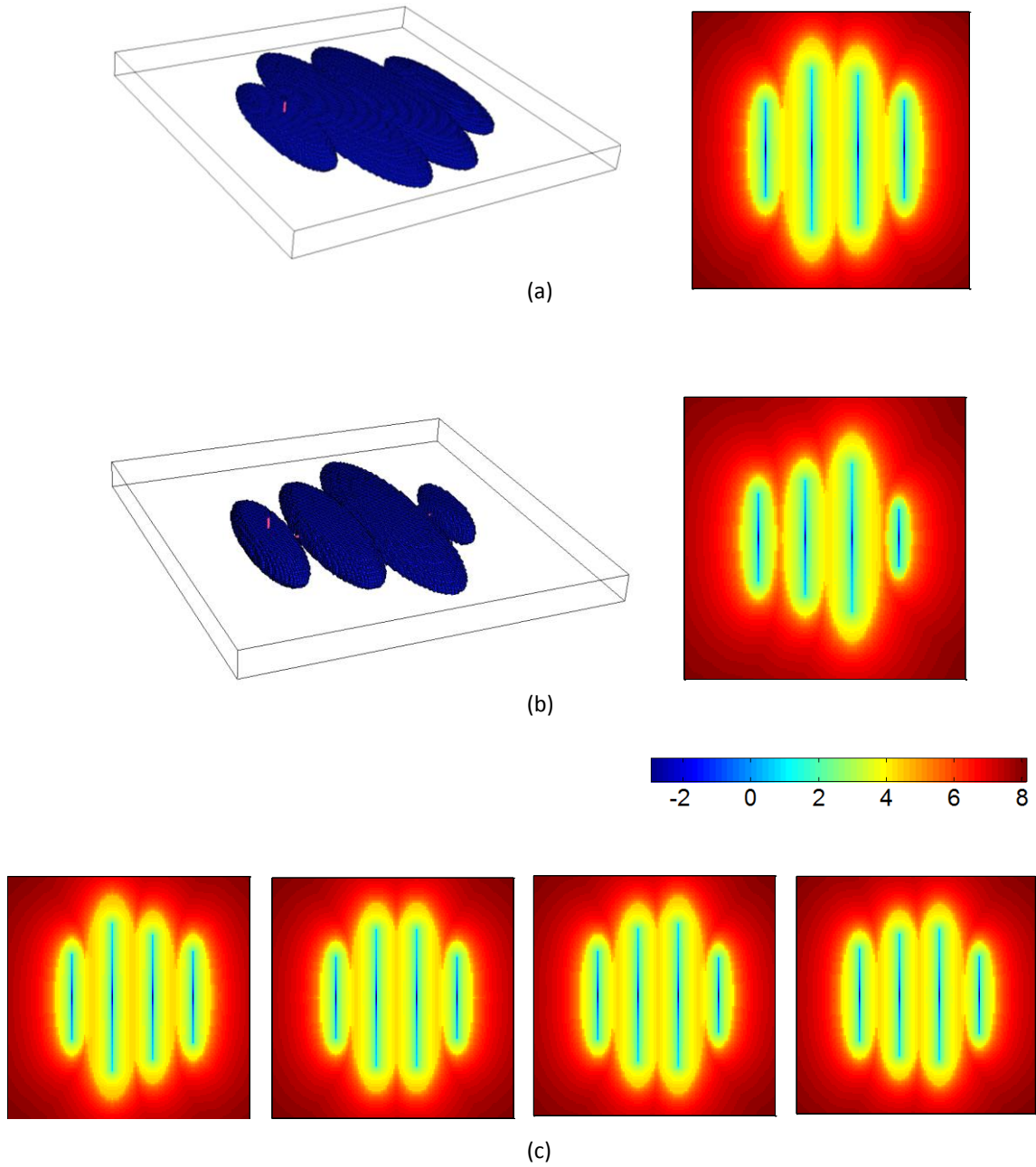


Figure 3.10: Graphical summary of history matching results showing (a) the EPA and logarithm of $\tau(\mathbf{x})$ for the reference model, (b) the EPA and logarithm of $\tau(\mathbf{x})$ for the base model, (c) logarithm of $\tau(\mathbf{x})$ for 4 models sampled from the posterior distribution

3.4 Summary

In this chapter, we focused on solving an important problem in reservoir characterization – history matching and uncertainty analysis. We considered a tight oil reservoir history matching problem by integrating the well bottomhole pressure (BHP) data to reduce uncertainties in model parameters. We approached the problem in the Bayesian framework using the Markov Chain Monte Carlo (MCMC) method. We compared the efficiency of the single stage (normal) MCMC algorithm with a two-stage MCMC algorithm which required an efficient proxy with which sampled models were quickly evaluated before running full scale simulations. We applied the Fast Marching Method (FMM) geometric pressure approximation as a proxy to quickly calculate the well BHP of each sampled model in the first stage of the two-stage MCMC algorithm. The suitability of the FMM-based proxy was confirmed for this problem as the acceptance rate in the two-stage MCMC improved 3 times over what was obtained with the single stage MCMC algorithm, without significant reduction in convergence rate.

CHAPTER IV

CONCLUSIONS AND RECOMMENDATIONS

In this work, we have applied the Fast Marching Method (FMM) to significantly improve the computational efficiencies associated with important hydrocarbon reservoir characterization tasks including geologic model ranking, reservoir model calibration and uncertainty analysis.

First, we demonstrated the application of the drainage volume, calculated using FMM, as a dynamic measure of reservoir performance and surrogate parameter in ranking multiple geologic models based on the cumulative oil production in conventional reservoirs under primary depletion. The concept was demonstrated for both 2D and 3D heterogeneous reservoirs.

Also a new approach, called the Gaussian quadrature method, for point-discretizing the surrogate parameter probability distribution function (PDF) was compared with traditional (P5-P50-P95 and P10-P50-P90) model selection methods. In our work, the Gaussian quadrature performed much better than the traditional methods in closely matching the true PDF of the actual reservoir performance parameter. However, it should be pointed out that, since the Gaussian quadrature model selection method is not based on predefined percentiles like the traditional methods, it may be difficult to identify specific percentile models, such as the P10 model, for instance. However, the Gaussian quadrature approach offers more advantages over the traditional methods if the primary goal of the model ranking task is to quickly and more accurately estimate the bounds of uncertainty without making Gaussianity assumptions.

Second, we considered an inverse problem involving a hydraulically fractured tight oil reservoir model calibration. The problem was approached in the Bayesian framework using the Markov

Chain Monte Carlo (MCMC) algorithm. The FMM was applied in the geometric pressure approximation as a proxy to quickly calculate the well bottomhole pressure (BHP) and thus, evaluate proposal models in the first stage of a two-stage MCMC algorithm, before running full simulations in the second stage. The performances of the two-stage and single stage MCMC algorithms were compared. The two-stage MCMC algorithm was found to be about *3 times* faster than the single stage MCMC algorithm with the same level of uncertainty reduction and without substantial decrease in convergence rate. This was as a result of the suitability of the FMM-based proxy in evaluating the proposal models.

The two-stage MCMC algorithm gave better estimation of parameters, especially for the matrix permeability and the hydraulic fracture half-lengths. This is due to the fact that the two-stage MCMC algorithm could sample more from the posterior distribution with 500 iterations than the single stage MCMC due to the much higher second stage acceptance rate. The fracture permeability was however poorly estimated by both algorithms. This can be attributed to the low sensitivity of this parameter due to the high value.

A good direction towards achieving more robustness with this technique is to consider the formulation of the FMM-based proxy to effectively handle BHP constrained wells as well as wells with varying rates including multiphase flow systems. Improving the robustness will also require adapting the FMM algorithm to handle anisotropic permeability fields as well as corner point and unstructured gridding.

An attempt was also made in this work on the application of FMM geometric pressure approximation in obtaining steady state pressure solutions for conventional reservoirs as presented in the Appendix A of this thesis. It was discovered that the approximations were closer to true solutions for homogeneous than for heterogeneous reservoirs. Also, for transient

pressures in unconventional reservoirs with multistage transverse hydraulic fractures, it was slightly more efficient to calculate the pressure field with iterative solvers using an initial guess obtained from FMM geometric pressure approximation than using a homogeneous pressure field. To further improve the effectiveness of the FMM pressure approximation initial guess, it will be worthwhile to adapt the FMM algorithm to handle high heterogeneity contrasts that come with hydraulic fracture models.

REFERENCES

- Aanonsen, S.I., Nævdal, G., Oliver, D.S., Reynolds, A.C., and Vallès, B. 2009. The Ensemble Kalman Filter in Reservoir Engineering -- A Review. *SPE Journal* **14** (3): pp. 393-412. SPE-117274-PA.
- Al-Khalifa, M.A. 2004. Advances in Generating and Ranking Integrated Geological Models for Fluvial Reservoir. Presented at the SPE Asia Pacific Conference on Integrated Modelling for Asset Management. 00086999.
- Alabert, F.G. and Modot, V. 1992. Stochastic Models of Reservoir Heterogeneity: Impact on Connectivity and Average Permeabilities. Presented at the SPE Annual Technical Conference and Exhibition. 00024893.
- Ambrose, R.J., Clarkson, C.R., Youngblood, J.E., Adams, R., Nguyen, P.D., Nobakht, M., and Biseda, B. 2011. Life-Cycle Decline Curve Estimation for Tight/Shale Reservoirs. Presented at the SPE Hydraulic Fracturing Technology Conference. SPE-140519-MS.
- Bello, R.O. and Wattenbarger, R.A. 2010. Multi-Stage Hydraulically Fractured Horizontal Shale Gas Well Rate Transient Analysis. Presented at the North Africa Technical Conference and Exhibition. SPE-126754-MS.
- Christian, J.T. and Baecher, G.B. 1999. Point-Estimate Method as Numerical Quadrature. *Journal of Geotechnical and Geoenvironmental Engineering* **125** (9): 779-786.
- Cipolla, C.L., Lolon, E., Erdle, J., and Tathed, V.S. 2009. Modeling Well Performance in Shale-Gas Reservoirs. Presented at the SPE/EAGE Reservoir Characterization and Simulation Conference. SPE-125532-MS.
- Cipolla, C.L., Mack, M.G., and Maxwell, S.C. 2010. Reducing Exploration and Appraisal Risk in Low Permeability Reservoirs Using Microseismic Fracture Mapping - Part 2. Presented at the SPE Latin American and Caribbean Petroleum Engineering Conference. SPE-138103-MS.
- Cipolla, C.L., Weng, X., Mack, M.G., Ganguly, U., Gu, H., Kresse, O., and Cohen, C.E. 2011. Integrating Microseismic Mapping and Complex Fracture Modeling to Characterize Fracture Complexity. Presented at the SPE Hydraulic Fracturing Technology Conference. SPE-140185-MS.

- Datta-Gupta, A. and King, M.J. 2007. *Streamline Simulation: Theory and Practice*. Society of Petroleum Engineers Richardson, TX.
- Datta-Gupta, A., Kulkarni, K.N., Yoon, S., and Vasco, D. 2001. Streamlines, Ray Tracing and Production Tomography: Generalization to Compressible Flow. *Petroleum Geoscience* **7**: 75-86.
- Datta-Gupta, A., Xie, J., Gupta, N., King, M.J., and Lee, W.J. 2011. Radius of Investigation and Its Generalization to Unconventional Reservoirs. *Journal of Petroleum Technology* **63** (7): 52-55.
- Deutsch, C.V. and Srinivasan, S. 1996. Improved Reservoir Management through Ranking Stochastic Reservoir Models. Presented at the SPE/DOE Improved Oil Recovery Symposium. 00035411.
- Dong, Z., Holditch, S., McVay, D., and Ayers, W. 2012. Global Unconventional Gas Resource Assessment. *SPE Economics & Management* **4** (4): 222-234.
- Du, C., Zhang, X., Zhan, L., Gu, H., Hay, B., Tushingham, K., and Ma, Y.Z. 2010. Modeling Hydraulic Fracturing Induced Fracture Networks in Shale Gas Reservoirs as a Dual Porosity System. Presented at the International Oil and Gas Conference and Exhibition in China. SPE-132180-MS.
- Du, C.M., Zhan, L., Li, J., Zhang, X., Church, S., Tushingham, K., and Hay, B. 2011. Generalization of Dual-Porosity-System Representation and Reservoir Simulation of Hydraulic Fracturing-Stimulated Shale Gas Reservoirs. Presented at the SPE Annual Technical Conference and Exhibition. SPE-146534-MS.
- Efendiev, Y., Datta-Gupta, A., Ginting, V., Ma, X., and Mallick, B. 2005. An Efficient Two-Stage Markov Chain Monte Carlo Method for Dynamic Data Integration. *Water Resources Research* **41** (12): W12423.
- Efendiev, Y., Hou, T., and Luo, W. 2006. Preconditioning Markov Chain Monte Carlo Simulations Using Coarse-Scale Models. *SIAM Journal on Scientific Computing* **28** (2): 776-803.
- Ertekin, T., Abou-Kassem, J.H., and King, G.R. 2001. *Basic Applied Reservoir Simulation*. Society of Petroleum Engineers Richardson, TX.

- Fatemi, E., Engquist, B., and Osher, S. 1995. Numerical Solution of the High Frequency Asymptotic Expansion for the Scalar Wave Equation. *Journal of Computational Physics* **120** (1): 145-155.
- Ge, J. and Ghassemi, A. 2011. Permeability Enhancement in Shale Gas Reservoirs after Stimulation by Hydraulic Fracturing. Presented at the 45th U.S. Rock Mechanics / Geomechanics Symposium. ARMA-11-514.
- Gildin, E., Valko, P., and Fuentes-Cruz, G. 2013. Analyzing Production Data from Hydraulically Fractured Wells: The Concept of Induced Permeability Field. Presented at the 2013 SPE Hydraulic Fracturing Technology Conference. SPE-163843-MS.
- Graf, T., Zangl, G., May, R.S., Hartlieb, M., Randle, J.M., and Al-Kinani, A. 2011. Candidate Selection Using Stochastic Reasoning Driven by Surrogate Reservoir Models. *SPE Reservoir Evaluation & Engineering* **14** (4): pp. 413-422. SPE-136373-PA.
- Gupta, N. 2012. A Novel Approach for the Rapid Estimation of Drainage Volume, Pressure and Well Rates. Master of Science, Texas A&M University.
- Hajizadeh, Y., Christie, M.A., and Demyanov, V. 2010. Comparative Study of Novel Population-Based Optimization Algorithms for History Matching and Uncertainty Quantification: PUNQ-S3 Revisited. Presented at the Abu Dhabi International Petroleum Exhibition and Conference. SPE-136861-MS.
- Hassouna, M.S. and Farag, A.A. 2007. Multistencils Fast Marching Methods: A Highly Accurate Solution to the Eikonal Equation on Cartesian Domains. *Pattern Analysis and Machine Intelligence, IEEE Transactions on* **29** (9): 1563-1574.
- Hastings, W.K. 1970. Monte Carlo Sampling Methods Using Markov Chains and Their Applications. *Biometrika* **57** (1): 97-109.
- Hill, A.C. and Thomas, G.W. 1985. A New Approach for Simulating Complex Fractured Reservoirs. Presented at the Middle East Oil Technical Conference and Exhibition. 00013537.
- Hird, K. and Dubrule, O. 1998. Quantification of Reservoir Connectivity for Reservoir Description Applications. *SPE Reservoir Evaluation & Engineering* **1** (1): 12-17.
- Hirsch, L. and Schuette, J. 1999. Graph Theory Applications to Continuity and Ranking in Geologic Models. *Computers & Geosciences* **25** (2): 127-139.

- Holditch, S.A. 2006. Tight Gas Sands. *Journal of Petroleum Technology* **58** (6): 86-93. SPE-103356-MS.
- Hosseini, S.A., Kang, S., and Datta-Gupta, A. 2010. Qualitative Well Placement and Drainage Volume Calculations Based on Diffusive Time of Flight. *Journal of Petroleum Science and Engineering* **75** (1): 178-188.
- Hu, L.Y., Ravalec, M.L., Blanc, G., Roggero, F., Noetinger, B., Haas, A., and Corre, B. 1999. Reducing Uncertainties in Production Forecasts by Constraining Geological Modeling to Dynamic Data. Presented at the SPE Annual Technical Conference and Exhibition. 00056703.
- Idrobo, E.A., Choudhary, M.K., and Datta-Gupta, A. 2000. Swept Volume Calculations and Ranking of Geostatistical Reservoir Models Using Streamline Simulation. Presented at the SPE/AAPG Western Regional Meeting. 00062557.
- Johns, R., Sepehrnoori, K., Varavei, A., and Moinfar, A. 2013. Development of a Coupled Dual Continuum and Discrete Fracture Model for the Simulation of Unconventional Reservoirs. Presented at the 2013 SPE Reservoir Simulation Symposium. SPE-163647-MS.
- Johnson Jr, C. 1956. Prediction of Oil Recovery by Waterflood-a Simplified Graphical Treatment of the Dykstra-Parsons Method. *Journal of Petroleum Technology* **8** (11): 55-56.
- Journel, A.G. 1990. Geostatistics for Reservoir Characterization. Presented at the SPE Annual Technical Conference and Exhibition. 00020750.
- Karimi-Fard, M., Durlofsky, L.J., and Aziz, K. 2003. An Efficient Discrete Fracture Model Applicable for General Purpose Reservoir Simulators. Presented at the SPE Reservoir Simulation Symposium. 00079699.
- Kazemi, H., Murrill Jr., L.S., Porterfield, K.L., and Zeman, P.R. 1976. Numerical Simulation of Water-Oil Flow in Naturally Fractured Reservoirs. *Society of Petroleum Engineers Journal* **16** (6): 317-326. 00005719.
- Kim, C.S. and Dobin, M.W. 2008. A Rapid Method for Reservoir Connectivity Analysis Using a Fast Marching Method. EP Patent 1,883,840.

- Lee, J., Rollins, J.B., and Spivey, J.P. 2003. *Pressure Transient Testing*. Richardson, Tex.: Henry L. Doherty Memorial Fund of AIME, Society of Petroleum Engineers.
- Luo, S., Wolff, M., Ciosek, J.M., Rasdi, M.F., Neal, L., Arulampalam, P., and Willis, S.K. 2011. Probabilistic Reservoir Simulation Workflow for Unconventional Resource Play: Bakken Case Study. Presented at the SPE EUROPEC/EAGE Annual Conference and Exhibition. SPE-142896-MS.
- Ma, X., Al-Harbi, M., Datta-Gupta, A., and Efendiev, Y. 2008. An Efficient Two-Stage Sampling Method for Uncertainty Quantification in History Matching Geological Models. *SPE Journal* **13** (1): pp. 77-87. SPE-102476-PA.
- Maucec, M., Douma, S.G., Hohl, D., Leguijt, J., Jimenez, E., and Datta-Gupta, A. 2007. Streamline-Based History Matching and Uncertainty -- Markov-Chain Monte Carlo Study of an Offshore Turbidite Oil Field. Presented at the SPE Annual Technical Conference and Exhibition. SPE-109943-MS.
- Mayerhofer, M.J., Lolon, E.P., Youngblood, J.E., and Heinze, J.R. 2006. Integration of Microseismic Fracture Mapping Results with Numerical Fracture Network Production Modeling in the Barnett Shale. Presented at the SPE Annual Technical Conference and Exhibition. SPE-102103-MS.
- Miller, A.C. and Rice, T.R. 1983. Discrete Approximations of Probability Distributions. *Management Science* **29** (3): 352-362.
- Mishra, S., Choudhary, M.K., and Datta-Gupta, A. 2000. A Novel Approach for Reservoir Forecasting under Uncertainty. Presented at the SPE Annual Technical Conference and Exhibition. 00062926.
- Mohaghegh, S.D., Liu, J.S., Gaskari, R., Maysami, M., and Olukoko, O.A. 2012. Application of Well-Base Surrogate Reservoir Models (SRMS) to Two Offshore Fields in Saudi Arabia, Case Study. Presented at the SPE Western Regional Meeting. SPE-153845-MS.
- Moinfar, A., Narr, W., Hui, M.-H., Mallison, B.T., and Lee, S.H. 2011. Comparison of Discrete-Fracture and Dual-Permeability Models for Multiphase Flow in Naturally Fractured Reservoirs. Presented at the SPE Reservoir Simulation Symposium. SPE-142295-MS.
- Moinfar, A., Varavei, A., Sepehrnoori, K., and Johns, R.T. 2012. Development of a Novel and Computationally-Efficient Discrete-Fracture Model to Study IOR Processes in Naturally Fractured Reservoirs. Presented at the SPE Improved Oil Recovery Symposium. SPE-154246-MS.

- Monteagudo, J. and Firoozabadi, A. 2004. Control-Volume Method for Numerical Simulation of Two-Phase Immiscible Flow in Two-and Three-Dimensional Discrete-Fractured Media. *Water Resources Research* **40** (7): W07405.
- Novlesky, A., Kumar, A., and Merkle, S. 2011. Shale Gas Modeling Workflow: From Microseismic to Simulation -- a Horn River Case Study. Presented at the Canadian Unconventional Resources Conference. SPE-148710-MS.
- Oliver, D.S., Reynolds, A.C., and Liu, N. 2008. *Inverse Theory for Petroleum Reservoir Characterization and History Matching*. Cambridge University Press.
- Remy, N. 2005. S-Gems: The Stanford Geostatistical Modeling Software: A Tool for New Algorithms Development. *Geostatistics Banff 2004*: 865-871.
- Rosenblueth, E. and Hong, H.P. 1987. Maximum Entropy and Discretization of Probability Distributions. *Probabilistic Engineering Mechanics* **2** (2): 58-63.
- Saad, N., Maroongroge, V., and Kalkomey, C.T. 1996. Ranking Geostatistical Models Using Tracer Production Data. Presented at the European 3-D Reservoir Modelling Conference. 00035494.
- Saad, Y. and Schultz, M.H. 1986. GMRES: A Generalized Minimal Residual Algorithm for Solving Nonsymmetric Linear Systems. *SIAM Journal on Scientific and Statistical Computing* **7** (3): 856-869.
- Samandarli, O., Ahmadi, H.A.A., and Wattenbarger, R.A. 2011. A Semi-Analytic Method for History Matching Fractured Shale Gas Reservoirs. Presented at the SPE Western North American Region Meeting. SPE-144583-MS. h
- Sehbi, B.S., Kang, S., Datta-gupta, A., and Lee, W.J. 2011. Optimizing Fracture Stages and Completions in Horizontal Wells in Tight Gas Reservoirs Using Drainage Volume Calculations. Presented at the North American Unconventional Gas Conference and Exhibition. SPE-144365-MS.
- Sethian, J.A. 1996. A Fast Marching Level Set Method for Monotonically Advancing Fronts. *Proceedings of the National Academy of Sciences* **93** (4): 1591-1595.
- Sethian, J.A. 1999. Fast Marching Methods. *SIAM Review* **41** (2): 199-235.

- Shook, G.M. and Mitchell, K.M. 2009. A Robust Measure of Heterogeneity for Ranking Earth Models: The F-Phi Curve and Dynamic Lorenz Coefficient. Presented at the SPE Annual Technical Conference and Exhibition. SPE-124625-MS.
- Srinivasan, S. and Caers, J. 2000. Conditioning Reservoir Models to Dynamic Data - A Forward Modeling Perspective. Presented at the SPE Annual Technical Conference and Exhibition. 00062941.
- Thompson, J.M., Mangha, V.O., and Anderson, D.M. 2011. Improved Shale Gas Production Forecasting Using a Simplified Analytical Method -- A Marcellus Case Study. Presented at the North American Unconventional Gas Conference and Exhibition. SPE-144436-MS.
- Vasco, D., Keers, H., and Karasaki, K. 2000. Estimation of Reservoir Properties Using Transient Pressure Data: An Asymptotic Approach. *Water Resources Research* **36** (12): 3447-3465.
- Virieux, J., Flores-Luna, C., and Gibert, D. 1994. Asymptotic Theory for Diffusive Electromagnetic Imaging. *Geophysical Journal International* **119** (3): 857-868.
- Warren, J.E. and Root, P.J. 1963. The Behavior of Naturally Fractured Reservoirs. *Old SPE Journal* **3** (3): 245-255.
- Xie, J., Gupta, N., King, M.J., and Datta-Gupta, A. 2012. Depth of Investigation and Depletion Behavior in Unconventional Reservoirs Using Fast Marching Methods. Presented at the SPE Europe/EAGE Annual Conference. SPE-154532-MS.
- Xie, J., Yang, C., Gupta, N., King, M.J., and Datta-Gupta, A. 2012. Integration of Shale Gas Production Data and Microseismic for Fracture and Reservoir Properties Using Fast Marching Method. Presented at the SPE Eastern Regional Meeting. SPE-161357-MS.
- Yin, J., Xie, J., Datta-gupta, A., and Hill, A.D. 2011. Improved Characterization and Performance Assessment of Shale Gas Wells by Integrating Stimulated Reservoir Volume and Production Data. Presented at the SPE Eastern Regional Meeting. SPE-148969-MS.
- Zhang, Y., Yang, C., King, M., and Datta-Gupta, A. 2013. Extension of Fast-Marching Methods to Corner Point and Unstructured Simulation Grids for Optimization of Unconventional Reservoir Developments. Presented at the 2013 SPE Reservoir Simulation Symposium. SPE-163637-MS.

APPENDIX A

APPLICATION OF FAST MARCHING METHODS TO PRESSURE FIELD CALCULATIONS

Over the years, technological boundaries in petroleum reservoir engineering have continually been shifted towards reducing computational time and improving the overall efficiencies in reservoir simulations. In this work we made efforts to accomplish a similar objective. Here, an application of Fast Marching Methods (FMM) for calculation of pressure field in both conventional and unconventional reservoirs is presented. The pressure field is estimated using the FMM geometric pressure approximation (Xie, Gupta, et al., 2012) and this is input as an initial guess into a linear system solver to obtain the full pressure field. The Generalized Minimal Residual Algorithm (GMRES) (Saad and Schultz, 1986) was adopted to solve the linear system.

Obtaining the approximate (guess) pressure field requires performing the geometric pressure approximation for each source and/or sink, having calculated the drainage volumes V_p as a function of time $t(\tau)$ using FMM; where τ refers to the diffusive time of flight with reference to each well. These pressure fields obtained with reference to each well are combined using the principle of superposition in space (Lee et al., 2003). For varying boundary conditions, such as step changes in rate schedules, the superposition in time principle is also applied. The approximate pressure fields are then provided as an initial guess into a linear system of equations which is constructed using a Finite Difference (FD) scheme (Ertekin et al., 2001) to be solved using the GMRES solver.

The results presented here are all based on rate constrained wells. For conventional reservoir cases, pressure fields are calculated for five –spot injection patterns with the injector in the center and equidistant from all producers at the corners. The approximate pressure fields are compared with the GMRES results for three different rate schedules in both homogeneous and heterogeneous reservoirs. For unconventional reservoirs on the other hand, both approximate pressure fields and GMRES results are compared with the results from a commercial simulator (ECLIPSE®). Also the degree of efficiency in pressure calculation derivable from using the approximate pressure field as an initial guess is assessed.

A.1 Procedure for Pressure Field Calculations using FMM

The steps involved are outlined as follows:

A.1.1 Drainage Volume Calculations with FMM

Pressure front contours can be approximated by solving the expression obtained from retaining the high frequency terms of the asymptotic expansion of the pressure solution (Vasco et al., 2000). This expression, referred to as the Eikonal equation is given in **Eq. (1.5)** of the main text, can be solved efficiently using the FMM (Sethian, 1999) to obtain the diffusive time of flight contours $\tau(\mathbf{x})$. This can be converted to an approximate pressure front arrival time $t(\tau)$ by a $\tau - t$ transformation, for example, given by $t = \tau^2(\mathbf{x})/c$ (Ertekin et al., 2001), where c is the transformation factor that depends specifically on the flow regimes. The drainage volume V_p can then be calculated as a function of time using thresholds of $t(\tau)$ contours as described in **Eq. (2.3)** of the main text. A $V_p vs t(\tau)$ relationship is obtained for each well in the reservoir and

therefore for n wells, corresponding $[V_p - t(\tau)]_j$ relationships are obtained for each $[well]_j$, $\forall j = [1, n]$.

A.1.2 Geometric Pressure Approximation and Superposition in Space and Time

Similar to **Eq. (3.10)** in the main text, the pressure drawdown with respect to each well is approximated by an integration of the inverse of V_p , mathematically expressed as:

$$\Delta p_j^*(\mathbf{x}, t) \cong \frac{Q_{w_j}}{c_t} \int_{\psi_j}^{t_j} \frac{dt'}{V_{p_j}(t')} \quad (\text{A.1})$$

where $\psi_j = t_j|_{V_{p_j} = V_{p_{j\mathbf{x}}}}$ refers to the pressure arrival time at position \mathbf{x} in the domain considered and with respect to a specific j^{th} well; Q_{w_j} represents the j^{th} well rate. The convention adopted in this work is negative Q_{w_j} values for producer wells and positive Q_{w_j} values for injector wells. Varying rate schedules are handled using the superposition in time principle (Lee et al., 2003). Considering m rate schedules for the j^{th} well, the pressure drawdown may be approximated as follows:

$$\Delta p_j^*(\mathbf{x}, t) \cong \frac{Q_{w_j^1}}{c_t} \sum_{i=1}^m \left(\frac{Q_{w_j^i} - Q_{w_j^{i-1}}}{Q_{w_j^i}} \int_{\psi_j^i}^{\Delta t_j^i} \frac{dt'}{V_{p_j}(t')} \right) \quad (\text{A.2})$$

where $Q_{w_j^i}$ refers to the rate at the i^{th} schedule. Here, we set $Q_{w_j^{i-1}} = 0$ when $i = 1$, so that $Q_{w_j^1}$ represents the first well rate. Also Δt_j^i represents the difference between the entire operation time

for the j^{th} well t_j and the time elapsed between the start of well operation to the i^{th} schedule t_j^i (that is $\Delta t_j^i = t_j - t_j^i$); and $\psi_j^i = \Delta t_j^i \Big|_{V_{p_j} = V_{p_{jx}}}$.

Pressure domains involving multiple wells can also then be handled using the superposition in space concept (Lee et al., 2003). In this work, the pressure field as a function of time $p^*(\mathbf{x}, t)$ may be obtained by summing up the pressure drawdowns approximated for each well, $\Delta p_j^*(\mathbf{x}, t)$ and subtracting the initial pressure field $p_{init}(\mathbf{x}, 0)$ as shown below:

$$p^*(\mathbf{x}, t) = p_{init} + \sum_{j=1}^n \Delta p_j^*(\mathbf{x}, t) \quad (\text{A.3})$$

A.1.3 Derivation of Linear System of Equations for GMRES Solver

This section revises the conventional Finite Difference (FD) discretization of the material balance equation in flow in porous media. The material balance equation for a single phase oil flow in porous media, neglecting gravity effects may be written as:

$$\frac{\partial}{\partial t} \left(\frac{\phi}{B_o} \right) = \nabla \cdot \left(\frac{1}{\mu B_o} \mathbf{k} \cdot \nabla p \right) + Q \quad (\text{A.4})$$

Using a simple FD scheme, the material balance can be re-expressed as:

$$\mathbf{C} \frac{d\mathbf{P}}{dt} = \mathbf{C} \left(\frac{\mathbf{P}^{n+1} - \mathbf{P}^n}{\Delta t} \right) = \mathbf{T} \mathbf{P}^{n+1} + \mathbf{Q} \quad (\text{A.5})$$

where, \mathbf{P}^{n+1} and \mathbf{P}^n are vectors containing pressure value of every grid cell at the current and old time steps respectively. The source and sink terms are placed in the vector \mathbf{Q} and the time

step size is given by Δt . The accumulation term on the left hand side of **Eq. (A-4)** for every grid cell are placed along the diagonal of the diagonal matrix C . For this problem the accumulation term form each grid cell is calculated as follows:

$$C_{i,j,k} = \frac{\phi_{i,j,k} c_t \Delta V}{5.615}; \quad \Delta V = \Delta x \Delta y \Delta z \quad (\text{A.6})$$

where total compressibility c_t is the sum of oil compressibility c_o and formation compressibility c_f . Also to simplify the simulations, the lagging coefficient method was adopted in constructing the linear system of equations. Thus the flux balance in each grid cell (first term on the right hand side of **Eq. (A-5)**) can be expressed as:

$$\begin{aligned} Flux_{i,j,k} = (\mathbf{TP})_{i,j,k} = & T_{i+1/2,j,k} (p_{i+1,j,k} - p_{i,j,k}) + T_{i-1/2,j,k} (p_{i-1,j,k} - p_{i,j,k}) \\ & + T_{i,j+1/2,k} (p_{i,j+1,k} - p_{i,j,k}) + T_{i,j-1/2,k} (p_{i,j-1,k} - p_{i,j,k}) \\ & + T_{i,j,k+1/2} (p_{i,j,k+1} - p_{i,j,k}) + T_{i,j,k-1/2} (p_{i,j,k-1} - p_{i,j,k}) \end{aligned} \quad (\text{A.7})$$

where the inter-cell transmissibility, evaluated at old time level n is obtained as:

$$T_{i\pm 1/2,j,k} = 0.001127 \frac{\Delta y \Delta z}{\Delta x} \frac{k_{x_{i\pm 1/2}}}{(\mu_o B_o)_{i\pm 1/2}} \quad (\text{A.8})$$

$$\text{with } k_{x_{i\pm 1/2}} = \left[\frac{1}{2} \left(\frac{1}{k_{x_i}} + \frac{1}{k_{x_{i+1}}} \right) \right]^{-1}$$

The inter-cell values for the viscosity μ_o and formation volume factor B_o are calculated as the arithmetic average of values in adjacent grid cells. Finally, solving for pressure at the new time level, we obtain:

$$(\mathbf{C}/\Delta t - \mathbf{T})\mathbf{P}^{n+1} = (\mathbf{C}\mathbf{P}^n/\Delta t + \mathbf{Q}) \quad (\text{A.9})$$

This can be written in the form:

$$\mathbf{A}\mathbf{P}^{n+1} = \mathbf{B} \quad (\text{A.10})$$

So that $\mathbf{P}^{n+1} = \mathbf{A}^{-1}\mathbf{B}$ essentially. However, to solve Eq. (A.10) more efficiently, iterative solvers are good choices in many cases. For this work, we apply the GMRES algorithm in MATLAB[®] specifying the approximate pressure field $p^*(\mathbf{x}, t)$ obtained from the FMM-geometric pressure approximation described earlier as an initial guess at the start of the iterative process.

A.2 Results and Discussion

In this section we present first, the results of the steady state pressure field calculations for conventional five-spot pattern in both homogeneous and heterogeneous waterflood reservoirs. Next the results of the application of this concept on an unconventional (hydraulically fractured) reservoir will be presented. For all cases considered, constant rate boundary conditions were applied to all wells. We assumed oil PVT properties such as viscosity μ_o and formation volume factor B_o have weak dependence on pressure. Reservoir initial reservoir pressure was assumed homogeneous at $p_{init} = 3000\text{psi}$. Furthermore, since pressure drop and rate do not exactly vanish at the radius of investigation, an extra term $e^{-r/2}$ was included in the estimation of the drainage volume used in all pressure calculations to further improve the quality of the geometric pressure approximation (Gupta, 2012).

A.2.1 Steady State Pressure Solutions for Synthetic Waterflood Reservoir

For this case, both homogeneous and heterogeneous 2-Dimensional flow domains were studied. For each, the pressure field was solved in the single phase framework using the equations shown above. The total compressibility and fluid viscosity were considered constant. The general waterflood pattern used for this study together with the flow rate schedules for each well is shown in **Fig. A.1**.

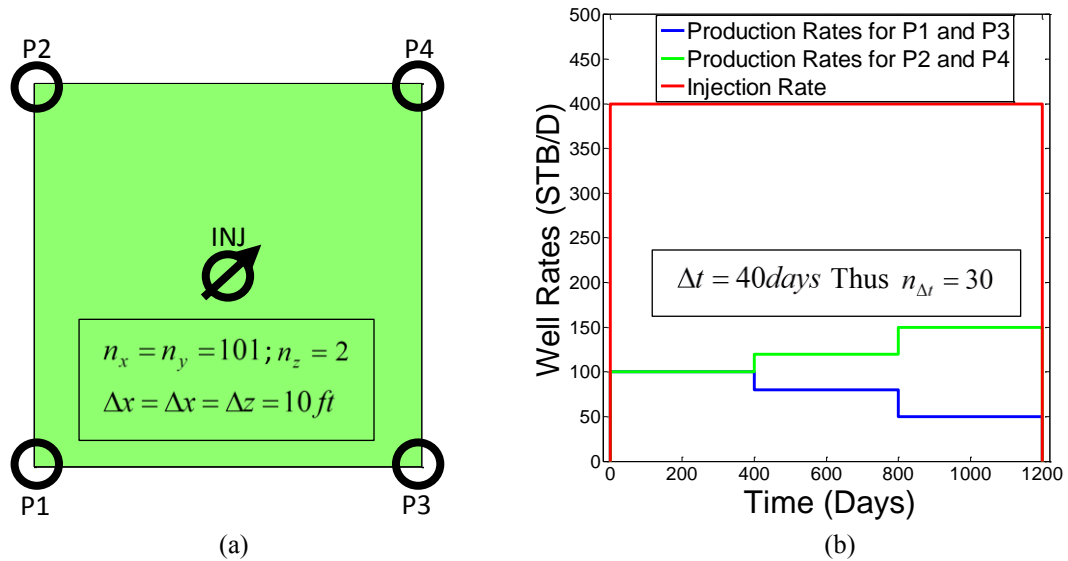


Figure A.1: Conventional reservoir test case set up showing (a) the waterflood pattern applied to both homogeneous and heterogeneous reservoirs and (b) well flow rate schedule

Homogeneous Reservoir Case

The results of the steady state pressure calculations for homogeneous permeability and porosity values of 100md and 0.1 is shown in **Fig. A.2**. Results at the 1st, 11th and 21st time steps are shown for FMM pressure solutions before and after refinements with GMRES. For intermediate

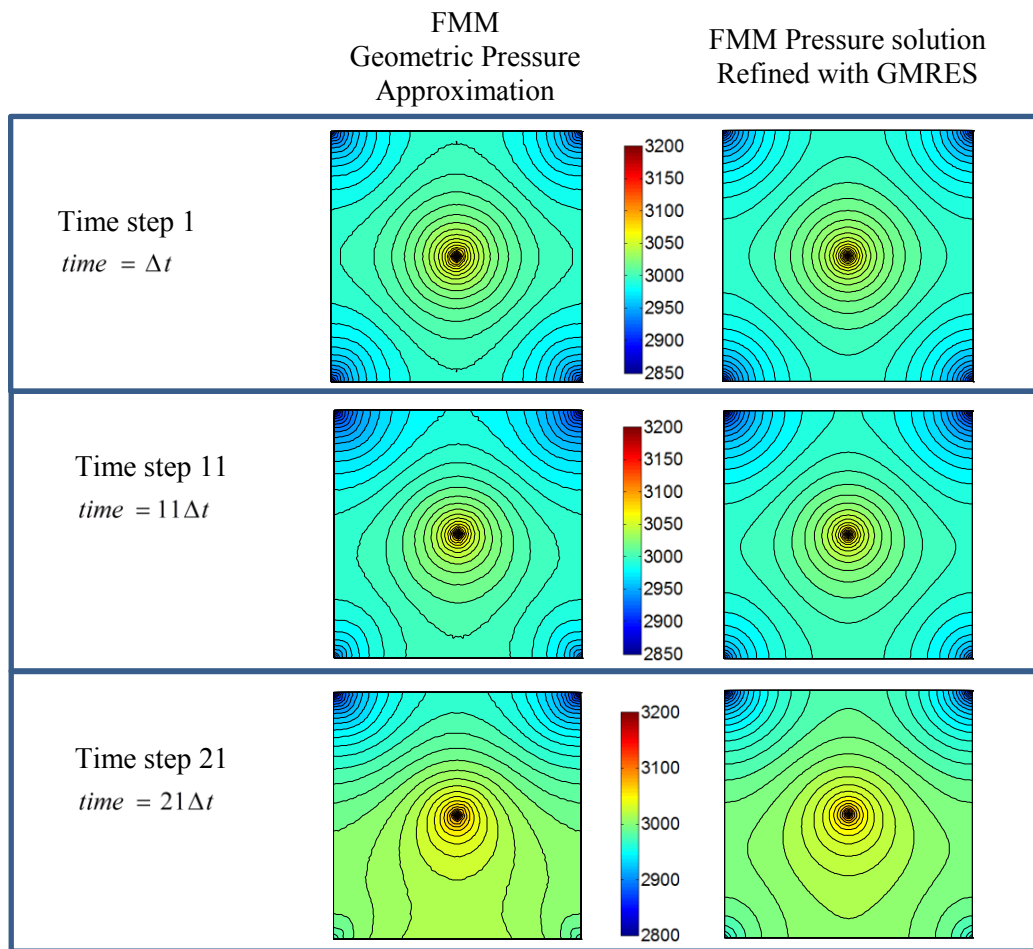


Figure A.2: Steady state FMM-approximate and GMRES-refined pressure solutions for homogeneous 5-spot waterflood pattern

time steps, rates well rates are constant and since the system is slightly compressible, pressure field changes are negligible. It is clear from the results that the pressure field obtained by FMM geometric approximation closely scales well with the refined (true) solution at all times. There are however, discrepancies in the shapes of the pressure contours especially when well rates differ significantly (at later time steps). This may be attributed to the fact that the FMM algorithm by nature does not properly handle the Neumann (no flux) boundary condition which was built into the system of equations for this problem. Therefore, FMM approximated pressure

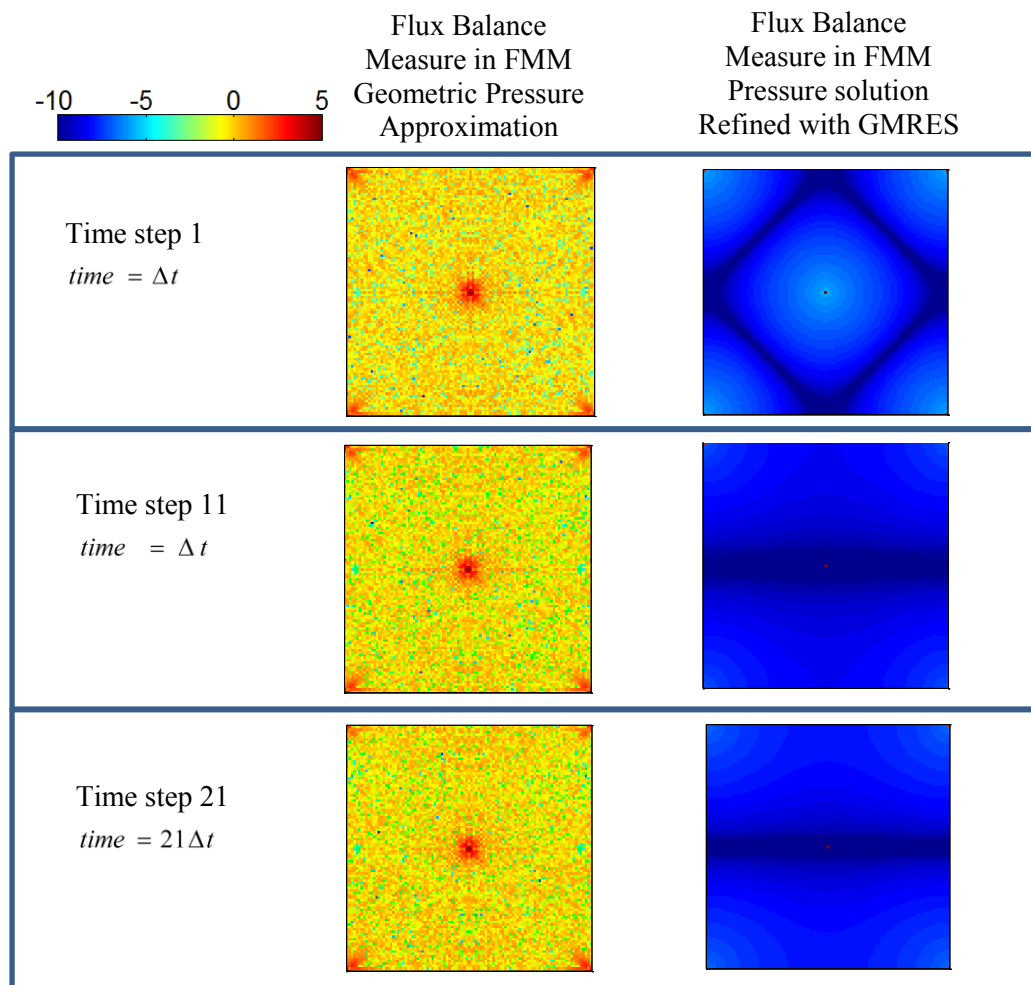


Figure A.3: Material balance errors in FMM-approximate and GMRES-refined pressure solutions for homogeneous 5-spot waterflood pattern

field contours are not normal to the boundaries as expected and as can be observed in the refined solutions. This implies artificial influxes at the boundaries which gives a possibility of local flux imbalance in each grid cell. The flux balance was quantified as a logarithm of the square of the divergence of flux calculated from Eq. A.7. The distributions of the flux balance for both approximate and refined solutions are shown in Fig. A.3. For slightly compressible flow, as we have in this problem, it is expected that flux balance should reduce to the (negligible) accumulation terms for all cells except at the wells. This can be observed with the true solutions

but not with the FMM approximate. Flux errors are randomly scattered throughout the domain while clustered around wells in the FMM approximate solutions.

Heterogeneous Reservoir Case

The results of the steady state pressure calculations using the heterogeneous permeability and porosity distributions shown in **Fig. A.4** are presented in **Fig. A.5**. Similar to the homogeneous case, results at the 1st, 11th and 21st time steps are shown for FMM pressure solutions before and after refinements with GMRES. Likewise, for intermediate time steps, the pressure field remains at steady state.

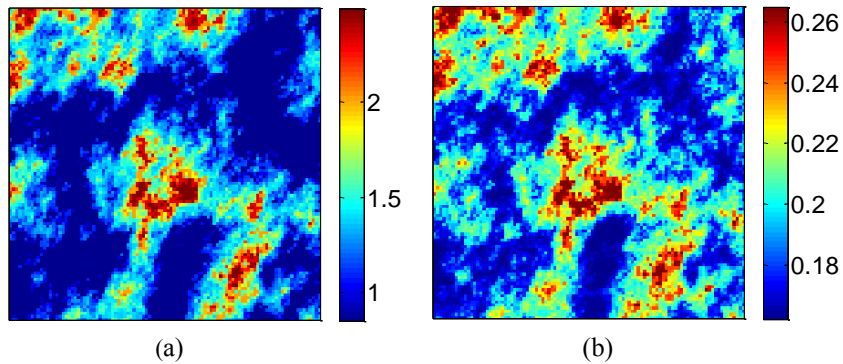


Figure A.4: Heterogeneous model: (a) permeability distribution on Logarithmic scale, (b) porosity distribution

Similar to the homogeneous reservoir case, FMM approximate pressure solutions do not satisfy the Neumann boundary condition so that pressure contours are not normal to the boundaries as shown in **Fig. A.5**. Aside that, in this case, FMM approximate pressure contours are dissimilar to the true pressure contours; although closely capture the actual ranges. Similar to the homogeneous case, the flux balances for both FMM approximate solutions and refined solutions are compared in **Figure A.6**.

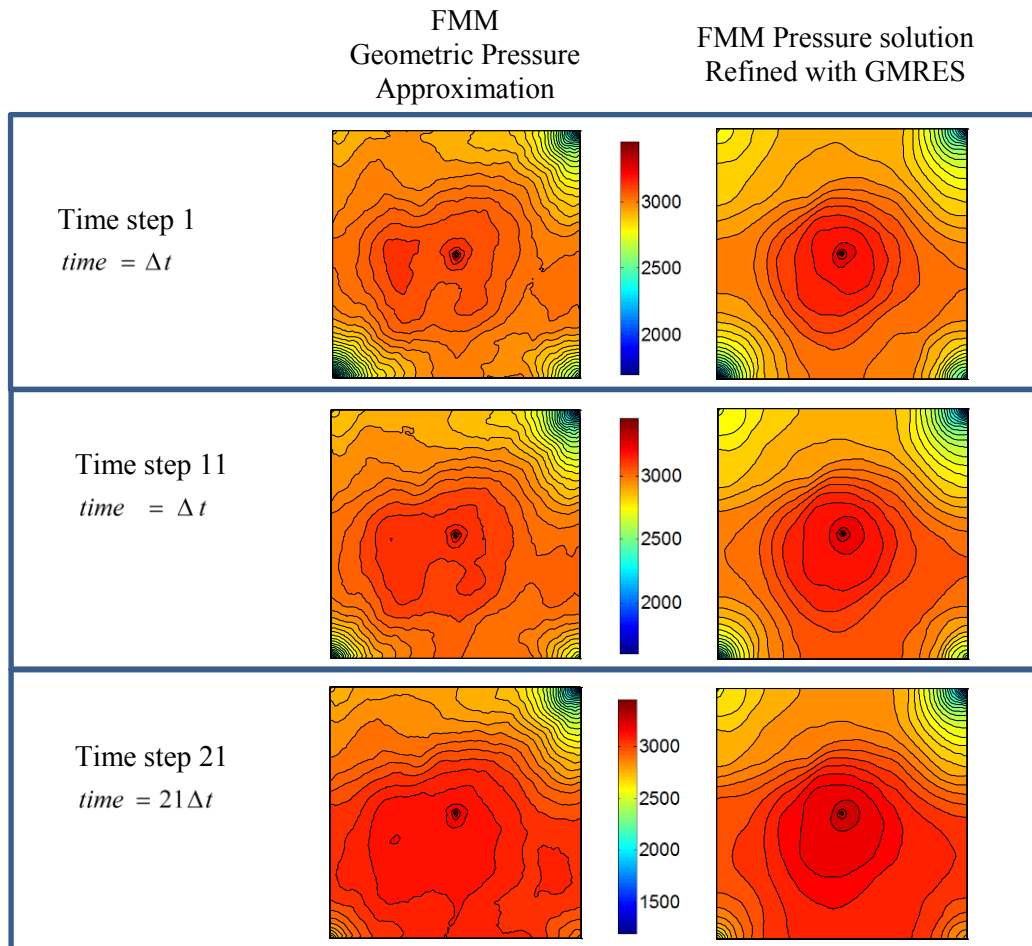


Figure A.5: Steady state FMM approximate and GMRES refined pressure solutions for heterogeneous 5-spot waterflood pattern

It is clear from this figure that flux errors get more significant both in high permeability regions and around well bore regions where flux magnitudes are high. This is also in agreement with the observation made in the homogeneous reservoir case where the high flux values occur only around well bore regions. The high values of the flux errors in high permeability regions cause artificial sinks/sources effects which can also be observed from the FMM approximate pressure contours.

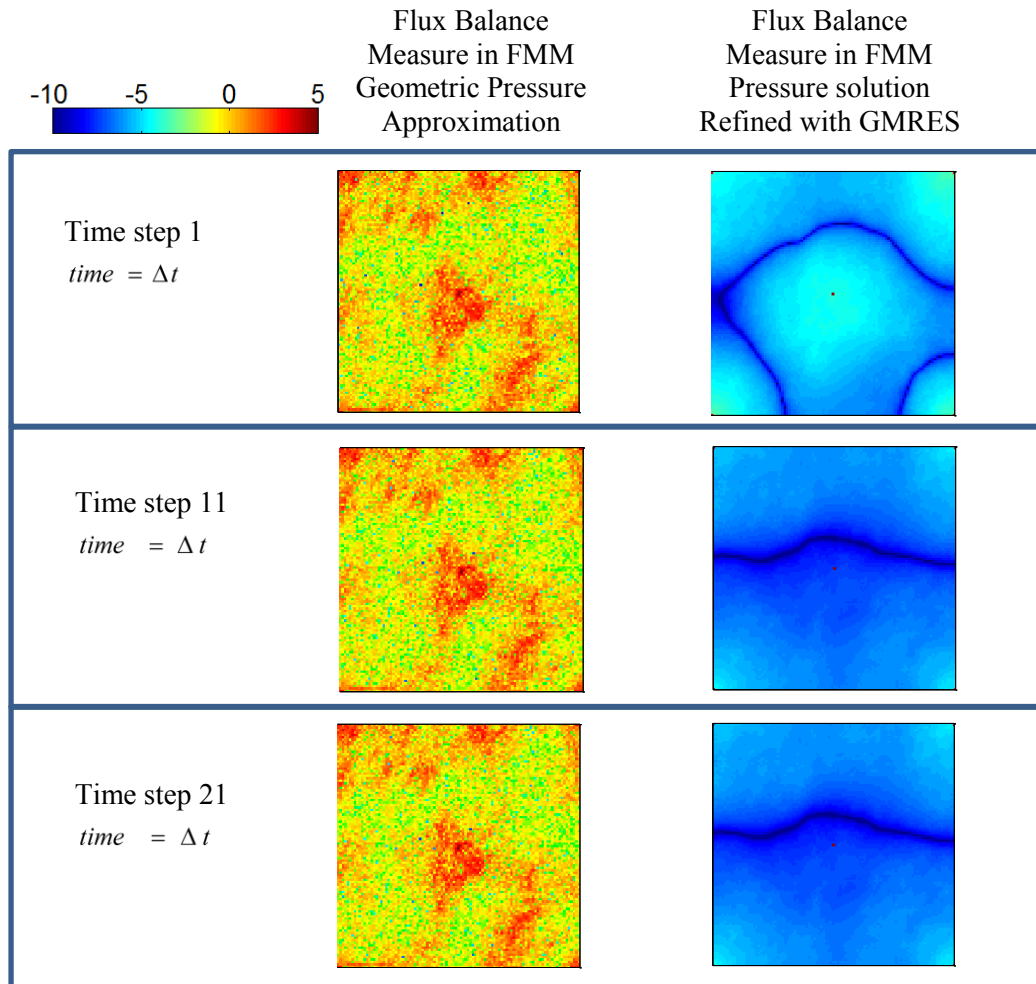


Figure A.6: Material balance errors in FMM approximate and GMRES refined pressure solutions for heterogeneous 5-spot waterflood pattern

Therefore it is safe to conclude here that increase in heterogeneity results in preferential clustering of flux imbalances in high permeability regions which, in turn deteriorates FMM geometric pressure approximations. Pressure solutions obtained by FMM pressure approximations are not perfect either for homogeneous flow media. Material balance errors are only almost evenly distributed throughout the medium so that sink/source artifacts are not formed.

A.2.2 Pressure Solutions for Unconventional (Tight) Reservoirs

For this study a synthetic homogeneous tight oil reservoir of matrix permeability $k_m = 0.05mD$ and porosity $\phi = 0.05$ was assumed to have slab geometry of size $4010 \times 8000 \times 50ft$, so that the reservoir could be finely discretized into $401 \times 800 \times 5$ grid cells of dimensions $10 \times 10 \times 10ft$. The reservoir was assumed to have been developed with a horizontal well completed with 5 transverse hydraulic fracture stages, equally spaced $1000ft$ apart and each of infinite conductivity. Each of the fracture stages similar fracture half-length $x_f = 550ft$ and fracture height spanning the whole pay zone. A constant rate boundary condition of $Q_w = 100bbl/D$ was applied to the well over a period of $10years$ ($3600days$).

The FMM approximate pressure solution at $10years$, shown in **Fig. A.7(a)** is compared with the pressure solution obtained from ECLIPSE[®] commercial simulator at the same time, shown in **Fig. A.7(b)**. From these figures, marked differences between the pressure distributions can be observed. This is as a result of the implicit assumption in FMM geometric pressure approximation that the $\tau(\mathbf{x})$ contours also define the pressure contours. The FMM approximated pressure distribution was also refined with the GMRES algorithm. However in this case, one of the goal was to compare the computational time required for GMRES to converge to the true solution at each time step with and without the FMM approximated pressure as initial guess.

For one test case, a homogeneous pressure distribution of $p_{init} = 3000psi$ was supplied as the initial guess, that is, $p_0(\mathbf{x}, t) = p_{init}$ at every time step; and for the second test case, the FMM approximated pressure calculated at the corresponding time step was supplied as the initial guess into GMRES, that is, $p_0(\mathbf{x}, t) = p^*(\mathbf{x}, t)$. The pressure distributions obtained from both cases are

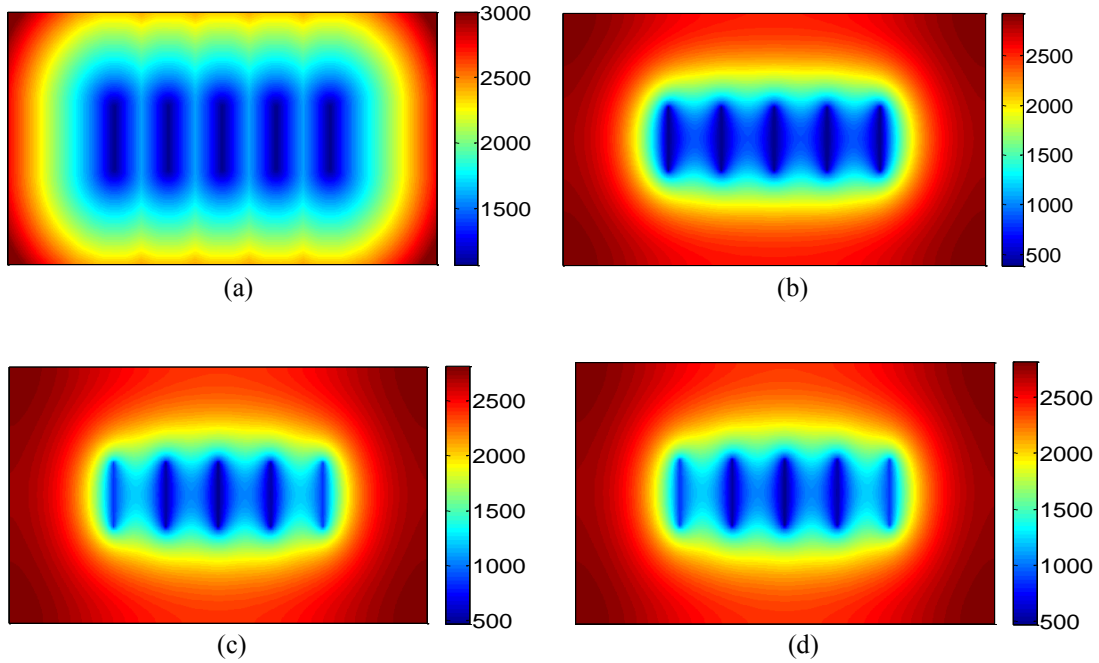


Figure A.7: Pressure solutions for a tight oil reservoir showing (a) FMM geometric approximation pressure distribution, (b) pressure distribution obtained from ECLIPSE[®], (c) GMRES pressure solution with $p_0(\mathbf{x},t) = p_{init}$, and (d) GMRES pressure solution with $p_0(\mathbf{x},t) = p^*(\mathbf{x},t)$

displayed in **Fig. A.7(c)** and **(d)** respectively. The pressure distributions obtained from the GMRES solutions also show close resemblance to the ECLIPSE[®] solution. As shown in **Fig. A.8**, the second approach of solving for the pressure distribution using the GMRES algorithm with the FMM approximated pressure distribution as the initial guess improves the computational speed of the calculation with increase in time. It should be noted that the pressure calculations are not done sequentially here. For instance, as shown in **Fig. A.8**, GMRES requires about 43seconds to obtain the pressure solution taking a single time step $\Delta t = 3200days$ from the initial homogeneous reservoir pressure distribution with initial guess $p_0(\mathbf{x},t) = p_{init}$, but 38seconds with same set up except with initial guess $p_0(\mathbf{x},t) = p^*(\mathbf{x},3200days)$.

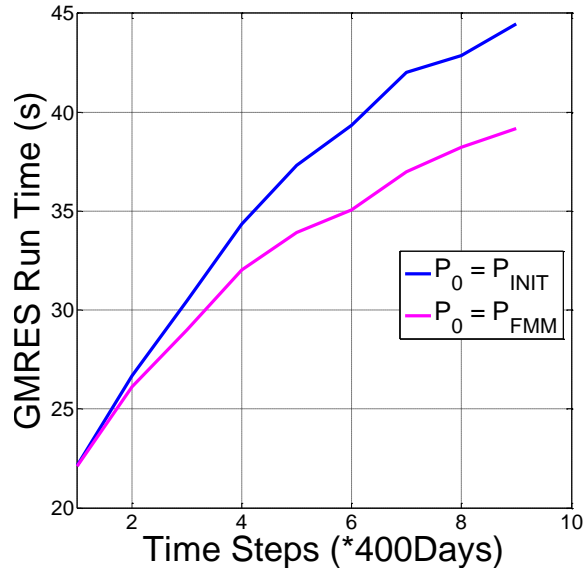


Figure A.8: Comparative GMRES computational time between cases:

$$p_0(\mathbf{x}, t) = p_{init} \text{ and } p_0(\mathbf{x}, t) = p^*(\mathbf{x}, t)$$

A.3 Summary

Here we have demonstrated another application of Fast Marching Methods (FMM) to reservoir pressure field calculations. The principle of superposition in time and space in the FMM geometric pressure approximation framework was also formulated and described. FMM approximated pressures were also refined with a GMRES solver. For conventional reservoirs under waterflood, FMM approximated steady state pressure solutions closely resemble the GMRES (finite difference) solutions even as rate schedules change. However, for the heterogeneous case, the pressure contours are distorted in FMM pressure approximations due to preferentially distribution of material balance errors.

For transient pressure solutions in hydraulically fractured tight reservoirs on the other hand, FMM approximate pressure solution also roughly captures the true range. Pressure contours however look different in shape compared with the contours in the true solutions. This is due to the formulation of the FMM geometric pressure approximation which assumes similar shapes of both the diffusive time of flight contours obtained from FMM and pressure contours. It was nonetheless observed that supplying the FMM pressure approximations as initial guesses to GMRES, especially for large time steps, reduces the pressure distribution computational time.